Quaternary Science Reviews 390 (2026) 110190

Contents lists available at ScienceDirect

Quaternary Science Reviews

journal homepage: www.elsevier.com/locate/quascirev

Evidence of a Weichselian MIS 3 proglacial lake south of Dogger Bank (southern North Sea)

Despina Kyriakoudi [a,b,*], Marc De Batist [b], Morgan Vervoort [a,b], Thomas Mestdagh [a], Tine Missiaen [a], Michael Grant [c], Tom Hill [d,e], Tim Kinnaird [f], Ruth Plets [a]

[a] Flanders Marine Institute (VLIZ), Ostend, Belgium
[b] Renard Centre of Marine Geology (RCMG) - Department of Geology, Ghent University, Ghent, Belgium
[c] Coastal and Offshore Archaeological Research Services, School of Ocean and Earth Science, National Oceanography Centre Southampton, University of Southampton, Waterfront Campus, European Way, Southampton, UK
[d] PalaeoEnvironmental Research and Consultancy Services (PERCS) Ltd, Princes Risborough, Buckinghamshire, UK
[e] School of Ocean and Earth Science, National Oceanography Centre, University of Southampton, Southampton, UK
[f] School of Earth and Environmental Sciences, University of St. Andrews, St. Andrews, UK

ARTICLE INFO

Handling Editor: Prof B Davies

Keywords:
North sea
Quaternary
Glaciation
Geomorphology
Lacustrine deposits
MIS 3

ABSTRACT

Offshore evidence for Weichselian glacial influence in the southern North Sea prior to the Last Glacial Maximum (LGM) remains sparse and discontinuously preserved, limiting reconstructions of ice extent and timing. Here, we present a detailed reconstruction of a previously unrecognised buried glaciolacustrine basin south of Dogger Bank, providing new insights into pre-LGM Weichselian glaciation. Integrated analysis of high-resolution 2D sub-bottom profiler data and sediment cores reveals a basin-like depocenter, covering a surface of ~69 km^2 and infilled by massive, fine-grained lacustrine sediments containing abundant ice-rafted debris, interpreted as dropstones. These deposits indicate sustained ice influence and sedimentation in an ice-proximal lake setting. Detailed, multi-method core analyses tightly constrain sediment accumulation to late Marine Isotope Stage (MIS) 3 (ca. 32-30 ka), yielding a high-resolution, directly dated offshore record of glacial influence in the southern North Sea before the LGM. The glaciolacustrine succession is locally overlain by glaciofluvial outwash deposits associated with LGM ice retreat (ca. 18 ka), while elsewhere it is truncated by younger Holocene incised channels and marine sediments. These findings support reconstructions placing a late MIS 3 ice margin in the study area and reveal a complex buried glaciated landscape of small, ice-proximal basins and ponds in the southern North Sea.

1. Introduction

The North Sea has experienced a long and complex Quaternary history marked by episodic basin erosion and infill, with its Pleistocene glacial history characterised by at least three major glacial stages over the past ca. 500 ka, namely the Elsterian/Anglian (MIS 12), the Saalian/Wolstonian (MIS 10-6), and the Weichselian/Devensian glaciation (MIS 5d-2) (e.g. Bradwell et al., 2008; Cameron et al., 1987, 1992; Ehlers, 1990; Graham et al., 2011; Kristensen et al., 2007; Ottesen et al., 2014; Scourse, 2024; Sejrup et al., 2000; Stoker et al., 2011). The Weichselian glaciation strongly shaped the North Sea region, yet the extent of the British-Irish Ice Sheet (BIIS) and the Fennoscandinavian Ice Sheet (FIS), their interactions and their evolution throughout this glaciation are still not fully understood (Cotterill et al., 2017a,b; Phillips et al., 2018; Roberts et al., 2018). An early phase of Weichselian ice-sheet growth is evidenced by records of grounded ice in the Fladen Basin and Norwegian Channel, indicating initial BIIS-FIS coalescence during MIS 4 (Carr et al., 2006; Graham et al., 2011; Mangerud, 2004; Sejrup et al., 2000). The latest phase, corresponding to the LGM, has been the focus of recent studies reconstructing the maximum ice extent in the North Sea, with models suggesting BIIS-FIS convergence between ~30 and 24 ka (Bradwell et al., 2008; Carr et al., 2006; Clark et al., 2022; Hughes et al., 2016; Sejrup et al., 2016). During this phase, when global sea level was ca. 130 m lower than present (Gibbard and Cohen, 2015; Lambeck et al., 2014) and large parts of the southern North Sea were exposed as an extensive lowland (Andresen et al., 2022;

* Corresponding author. Flanders Marine Institute (VLIZ), Ostend, Belgium.
E-mail address: despina.kyriakoudi@vliz.be (D. Kyriakoudi).

https://doi.org/10.1016/j.quascirev.2026.110190
Received 1 April 2026; Received in revised form 14 July 2026; Accepted 22 July 2026
Available online 25 July 2026
0277-3791/© 2026 The Authors. Published by Elsevier Ltd. This is an open access article under the CC BY license (http://creativecommons.org/licenses/by/4.0/).

Hughes et al., 2016), the ice margin extended over the present-day Dogger Bank area (Batchelor et al., 2019; Clark et al., 2022; Sejrup et al., 2016). The stratigraphy of Dogger Bank preserves the imprint of ice advance, expressed as repeated episodes of folding and thrusting linked to ice-lobe movement (Carr et al., 2006; Cotterill et al., 2017a, b; Emery et al., 2019; Phillips et al., 2022).

The existence of (large) proglacial lakes in the southern North Sea has long been hypothesised. These lakes are believed to have formed in response to ice-margin advance, ice-sheet coalescence and consequent drainage blockage, particularly during earlier Elsterian and Saalian glacial periods (Cohen et al., 2014; Hijma et al., 2012; Murton and Murton, 2012). More recent studies have also proposed the development of a proglacial lake along the southern ice margin near the Dogger Bank area, attributed to coalescence of the BIIS and FIS ice sheets during the LGM (MIS 2) (Murton and Murton, 2012; Sejrup et al., 2016). Support for the existence of a Late Weichselian lake at the LGM has been inferred from glacial lake outburst flood (GLOF) deposits, interpreted to record a catastrophic drainage of this lake towards the northeast through the Norwegian Channel at ca. 18.7 cal ka BP (Hjelstuen et al., 2018; Sejrup et al., 2016). However, direct sedimentological or geomorphological evidence constraining the existence, location, and spatial extent of such a Late Weichselian lake is still lacking (Murton and Murton, 2012). Records of analogous large proglacial lakes have nevertheless been documented onshore in the UK (e.g., lakes Wear and Humber), where they are interpreted to have been ice-dammed during the Late Weichselian (MIS 2) (Clark et al., 2004; Fairburn and Bateman, 2016; Murton et al., 2009).

Glaciolacustrine sediments are common in the geological record and are generally interpreted as evidence of ice-marginal or ice-fed proglacial lake development (Carrivick and Tweed, 2013; Ehlers and Linke, 1989; Eyles, 1987; Larsen et al., 2006; Livingstone et al., 2010). Proglacial lakes, formed at the margins of glaciers or ice sheets, are widespread and significant components of the Quaternary record, particularly during phases of deglaciation (Carrivick and Tweed, 2013). Elsewhere, well-documented ice-dammed lakes such as Lake Agassiz, Glacial Lake Missoula, and the Baltic Ice Lake demonstrate that large proglacial lakes are typically long-lived, extensive, and leave pronounced geomorphological and sedimentary signatures (Alho et al., 2010; Björck, 1995; Jensen et al., 1997; Teller et al., 2002). Their formation and dynamics are closely linked to climatic factors via surface energy balance, as well as to glacier dynamics, meltwater, and sediment fluxes (Larsen et al., 2011). An additional factor is glacio-isostatic adjustment (GIA), which drives earth deformation, spatially variable vertical land motion and relative sea-level change during and after deglaciation (Bradley et al., 2011, 2023). Sedimentation in these systems forms a key geochronological archive, recording meltwater variability from seasonal to longer timescales and providing proxy information on glacier mass balance, geometry, and behaviour, although such records may vary between catchments and across time (Carrivick and Chase, 2011; Carrivick and Tweed, 2013; Larsen et al., 2011; Phillips et al., 1996).

In this study, we reveal buried ice-proximal glaciolacustrine deposits south of Dogger Bank using high-resolution 2D sub-bottom profiler data and sediment cores (Fig. 1). A multi-proxy approach, combining sedimentological, geochemical, microfossil, and geochronological analyses, was applied to robustly characterise the geometry, stratigraphy, timing, and depositional setting of the lake deposits. These results provide rare offshore evidence of a relatively small MIS 3 glaciolacustrine lake in the southern North Sea (hereafter referred to as Lake Waldo, named after the WALDO project), documented in great detail, demonstrating that Weichselian ice-sheet influence extended into the region prior to the LGM. The study highlights the value of combining seismic and sedimentological datasets to reconstruct submerged glaciated landscapes, providing new insights into Early Weichselian (pre-LGM) ice-sheet dynamics in the southern North Sea.

2. Methods

An integrated dataset comprising high-resolution 2D sub-bottom profiler and sedimentological data was utilised. Data were collected onboard *RV Belgica* cruises BE2022-30 and BE2023-19 in 2022 and 2023, respectively (Fig. 1B).

2.1. Sub-bottom profiler data acquisition and processing

High-resolution sub-bottom profiles were collected using the hull-mounted parametric sub-bottom profiler TOPAS PS18 (Kongsberg), using central frequencies from 2.0 to 4.0 kHz (Ricker wavelet), a sampling rate of 64 kHz, recording window lengths of 120-130 ms and a constant ping interval of 200 ms. Acoustic data were processed using RadExPro 2022.4 software to enhance the signal-to-noise ratio (using bandpass, burst noise removal and 2D spatial filters) and apply vertical corrections for transducer depth and variations in tidal height. The latter correction was based on modelled sea surface heights at the time and location of acquisition, extracted from the *Atlantic-European North West Shelf Ocean Physics Analysis and Forecast* model (E.U. Copernicus Marine Service Information, 2023). These values, originally expressed in metres above the geoid (a close approximation of Mean Sea Level - MSL) were converted to metres above Lowest Astronomical Tide (LAT) using the MSL-LAT offset grids for the UK and Dutch continental shelves (respectively made available through the *ADMIRALTY Marine Data Portal* and the *Hydrographic Service of the Royal Netherlands Navy*). Tidal heights in m LAT were finally converted to two-way travel time (TWT) (assuming a velocity of 1500 m s^{-1} in seawater) and subtracted from the depths recorded in the acoustic data; as such, the vertical reference level shown in the profiles is LAT. Profiles were subsequently interpreted using the Kingdom™ Geoscience software (S&P Global, version 2023). Interpretations were performed in TWT, and an average velocity of 1600 m s^{-1} was applied for the depth conversion for the units below the seafloor (Andresen et al., 2022; Cotterill et al., 2017a,b; Hepp et al., 2017). The description of seismic facies was based on the terminology defined by Mitchum et al. (1977).

ArcGIS Pro 3.5.4 (Esri, 2025) was used to create and visualise spatial data and maps. Three-dimensional reconstruction was performed using the topo-to-raster interpolation method with a 50 m cell size to model the base of the lake sediments, which was subsequently used to derive key morphometric parameters, including the surface area and volume of sediments.

2.2. Sediment cores and analyses

Three sediment cores (DB_VC01, DB_VC02 and DB_VC03) were obtained during *RV Belgica* survey BE2023-19 in October 2023 from the area south of Dogger Bank (Fig. 1; Table 1). Cores were collected using an OSIL Vibrocorer system, with a maximum penetration depth of 4.5 m. Water depths were determined relative to LAT based on the acoustic profiles, assuming a constant sound velocity in water of 1500 m s^{-1}. Upon retrieval, cores were split under red light conditions to prevent photochemical alteration of sedimentary components and to facilitate sampling for OSL dating. Sedimentary structures and lithologies were documented through visual core logging and high-resolution digital core photography was performed at the Royal Netherlands Institute for Sea Research (NIOZ) using the AvaaTech core scanner. Archive and working halves are stored at the Marine Station Ostend (MSO) of the Flanders Marine Institute (VLIZ) under cool conditions. Malacological samples were examined along the sediment cores to provide a general indication of depositional conditions (F. Wesselingh, personal communication). More detailed sedimentological, geochemical, chronological and micropaleontological analyses were undertaken on DB_VC02 core.

Grain-size analysis

Grain-size analysis was conducted on core DB_VC02. Sediment

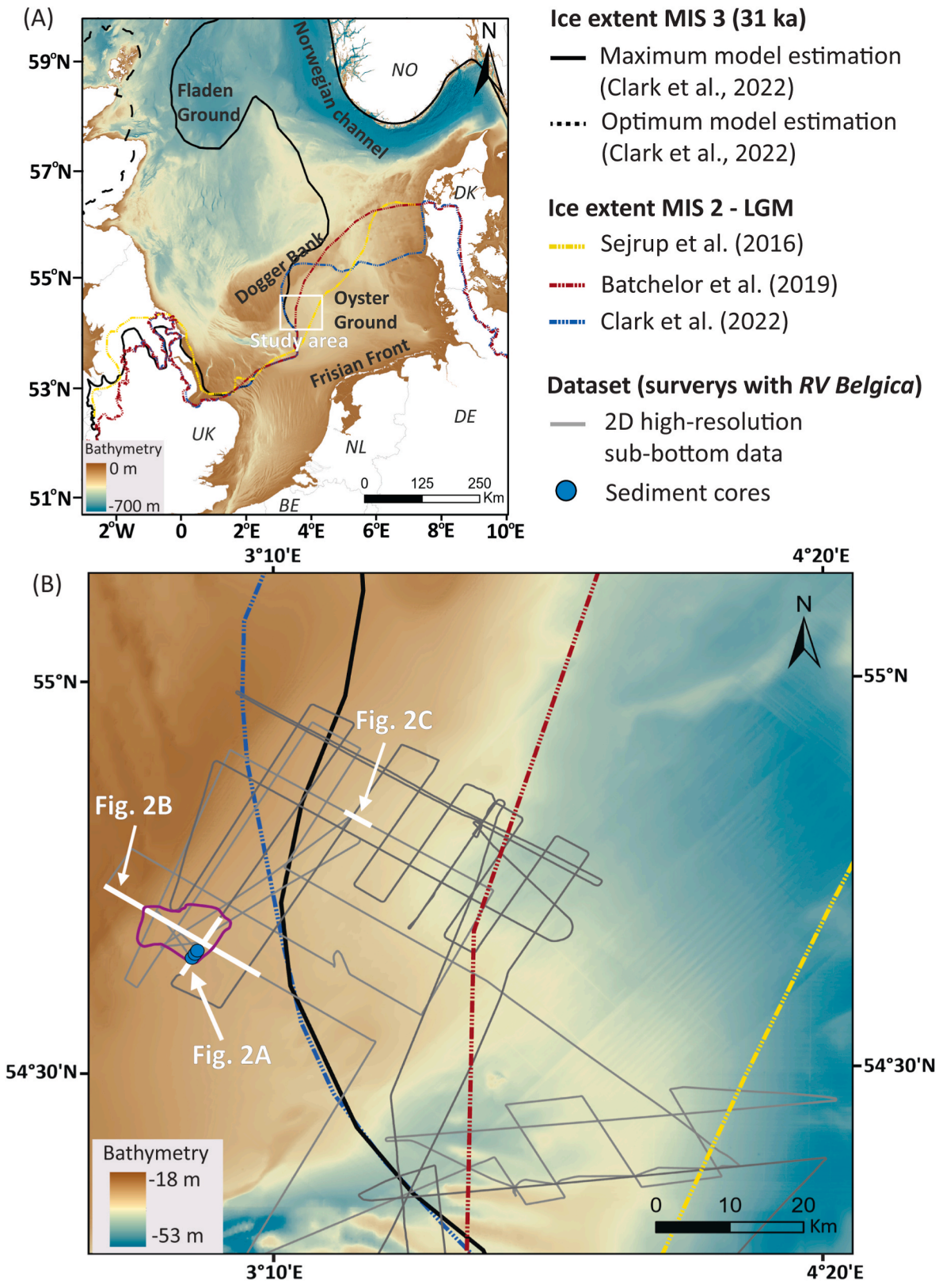


Fig. 1. (A) Map of the southern North Sea showing the study site south of Dogger Bank, outlined by a white polygon. Both optimal and maximum ice extents during MIS 3 (31 ka) are shown by solid and dashed black lines, respectively, based on models by Clark et al. (2022). Maximum LGM ice extents reconstructed by Sejrup et al. (2016), Batchelor et al. (2019) and Clark et al. (2022) are shown as coloured dashed lines. (B) Detail of (A), showing the location of high-resolution 2D sub-bottom profiler data (grey lines) and sediment cores (blue dots) collected during surveys with the *RV Belgica*. The purple polygon indicates the extent of the lake deposits mapped in this study (see Fig. 2A-B). Bathymetric data were obtained from the EMODnet Bathymetry portal.

Table 1
Details on the three vibrocores used in this study.

Full core name	Abbreviated core name	Date acquired	Latitude (N)	Longitude (E)	Core length (cm)	Seafloor depth (LAT) (m)[a]	Seafloor depth (MSL) (m)[b]
BE2023-19 DB_VC01	DB_VC01	9/10/2023	54.645745°	2.995222°	328	−36.3	−36.1
BE2023-19 DB_VC02	DB_VC02	9/10/2023	54.652744°	3.003236°	284	−36.6	−36.4
BE2023-19 DB_VC03	DB_VC03	9/10/2023	54.655395°	3.006266°	341	−36.7	−36.5

[a] Depths relative to Lowest Astronomical Tide (LAT), based on TOPAS acoustic profiles.
[b] Depths relative to mean sea level (MSL), referenced to the EMODnet bathymetry.

samples were collected at 4-5 cm intervals from ~110 to 280 cm depth and analysed at the Department of Geology of Ghent University. Samples were pre-treated to isolate the siliciclastic fraction, following the procedure of Van Daele et al. (2016), where organic matter was removed with H_2O_2, calcium carbonate with HCl and biogenic silica with NaOH. Grain-size distributions were measured using the Malvern Mastersizer 3000 laser diffraction analyser from Ghent University, and the results were processed in GRADISTAT (version 8.0) (Blott and Pye, 2001).

Additionally, fine-grained, silt-matrix sediments were wet-sieved to extract larger clasts from cores DB_VC02 and DB_VC03. The recovered clasts were examined macroscopically, and mineralogical determinations were subsequently performed.

X-ray fluorescence core scanning

X-ray fluorescence (XRF) core scanning was used as a non-destructive method to determine the elemental composition of the sediment. Measurements were carried out using an AvaaTech core scanner at NIOZ. The split core DB_VC02 (85-284 cm; sections 2/3 and 3/3) was scanned at 10 mm resolution, using a slit size of 1 mm downcore and 12 mm cross-core, with energy settings of 10 kV (0.3 mA, 5 s), 30 kV (0.2 mA, 5 s), and 50 kV (0.175 mA, 10 s). Further technical details and analytical specifications of the XRF core scanner are provided in Richter et al. (2006). To interpret the obtained geochemical data, centered log-ratio (clr) transformation and additive-log ratio (alr) were applied to the compositional data using statistical analyses in R software (RStudio 4.4.2) (Martin-Puertas et al., 2017; Weltje et al., 2015).

Microfossil analysis

Three samples for microfossil analysis were collected from core DB_VC02 at 135 cm, 213.5 cm, and 255 cm.

Pollen analysis was conducted at Coastal and Offshore Archaeological Research Services (COARS), UK, with pollen extraction undertaken at the Palaeoenvironment Laboratory, University of Southampton. Standard preparation procedures were followed (Moore et al., 1991), with 2-4 cm^3 of sediment processed per sample. All samples contained sufficient pollen, allowing counts of 149-202 total land pollen (TLP) to be achieved. Identifiable pollen and spore types were determined to the lowest possible taxonomic level, and pollen diagrams were plotted using Tilia software (version 3.0.3) (Grimm, 1991).

Samples for diatom assessment were processed at PalaeoEnvironmental Research and Consultancy Services, UK, using 1 cm^3 of sediment per sample. To assess whether diatoms were present in sufficient abundance, a count of up to 100 total diatom valves (TDV) was undertaken, whereas if diatoms were scarce, ten slide traverses were examined. Diatom identification was performed with reference to Hendy (1964), Krammer and Lange-Bertalot (1986-1991) and Van der Werff and Huls (1958-1974).

Sediment samples from DB_VC02 (section 3/3) and DB_VC03 (section 4/4) were examined to assess foraminiferal content. No foraminifera were observed in any of the samples.

Computed tomography scanning

Computed tomography (CT) scanning was conducted on split sections of core DB_VC02 at the Ghent University Hospital using a Siemens SOMATOM Definition Flash CT scanner (120 kV, effective mAs: 400). The scans were exported as DICOM file images (resolution: 0.15 mm/pixel, thickness: 0.6 mm) and stacked to generate 3D volumes. Using this non-destructive method, the internal structure of a sediment core could be examined at high resolution, allowing the distinction of density contrasts and sedimentary structures. The reconstructed images were imported into Dragonfly software (version 2024.1) for further visualisation, segmentation and measurements.

This software enables the isolation of voxels and the quantification of a range of their properties. Segmentation of coarser-sized clasts from the surrounding finer sediment matrix can be achieved by modifying the intensity thresholds, as each material is characterised by a specific range of Hounsfield Units (HU) values. HU provide a quantitative measure of attenuation in imaged materials, with values primarily determined by material density, making them useful for differentiating sediment types (Hounsfield, 1973; Reilly et al., 2017). In this study, the scale range was adjusted to 960-1900 HU, within which all sediment components were visible, while a dual threshold of 1680-1720 HU was applied to isolate the higher-density clasts from the finer material (clay, silt, fine sand), allowing the imaging and measurement of discrete clasts within the core. For all distinguished voxels corresponding to coarser-sized material, the equivalent spherical diameter (ESD) was calculated. The ESD represents the diameter of a sphere having the same volume as the irregular particle (Jennings and Parslow, 1988), serving as a primary parameter determining particle size (Thys et al., 2019). Particles with an ESD exceeding 0.25 mm (medium sand or coarser) are classified as debris particles, with the theoretical minimum detectable grain size (~0.24 mm) determined by the voxel resolution of the CT images (Nesje et al., 2007; Thys et al., 2019; Vasskog et al., 2011). Following segmentation, voxel-level measurements were extracted for each clast, including ESD, Feret diameters, volume, surface area, sphericity and principal axis orientation. These morphometric parameters were used to describe particle size, shape and orientation.

The clast morphology classification scheme used in this study was derived from established morphometric frameworks (Blott and Pye, 2008; Sneed and Folk, 1958; Zingg, 1935) and adapted for compatibility with the 0-1 scale given by Dragonfly software, resulting in four Aspect Ratio subgroups: $\geq$0.8 equant, 0.6-0.8 sub-equant, 0.3-0.6 elongated, and $<$0.3 platy or flattened. Sphericity values were similarly grouped, with an Aspect ratio $\geq$0.9 indicating high sphericity, 0.75-0.9 moderate, and $<$0.75 low to irregular sphericity. Orientation of the principal axis (θ) ranges from 180° to 180°, where the Rayleigh test assessed whether particle orientations were uniformly distributed, with R quantifying alignment (0 = random, 1 = perfect alignment). These groupings were established to facilitate comparison among samples and reflect the relative geometries described in classical shape classifications, while remaining consistent with 3D CT-based morphometric studies. Detailed definitions and computational details are provided in

supplementary material S1.

Radiocarbon dating

Radiocarbon dating was performed on intact *in situ* shell samples from the DB_VC01 core (see Table 2 for sample depths). Samples were submitted to *Beta Analytic Inc.* for accelerator mass spectrometry (AMS) analysis. Results are expressed as radiocarbon years before present (^{14}C a BP), where "present" is defined as AD 1950, and quoted uncertainties represent ±1σ counting statistics, rounded to the nearest 10 years following the conventions of the 1977 International Radiocarbon Conference. When calculated uncertainties were less than ±30 years, a minimum error of ±30 ^{14}C a BP was applied. δ^{13}C values are reported relative to the Vienna Pee Dee Belemnite (VPDB) standard. Calendar age calibration was undertaken in the OxCal program using the Marine20 calibration curve (Heaton et al., 2020) and the Bayesian probability method of Bronk Ramsey (2009). No additional local reservoir correction (ΔR) was applied to the shell dates (i.e. ΔR = 0), following the protocol proposed by Clark et al. (2022) for Holocene ages.

Optically stimulated luminescence dating

Depositional ages were obtained using Optically Stimulated Luminescence (OSL) from core DB_VC01 (321 cm) and core DB_VC02 (123.5 and 269.5 cm) (Table 3, Fig. 3). Cores were sampled under red-light conditions, and portable OSL equipment was used during sampling to screen the behaviour of bulk sediment throughout the core. The SUERC portable OSL reader was programmed with an interleaved measurement sequence of system dark count, infrared stimulated luminescence (IRSL) and OSL. From these measurements IRSL and OSL net signal intensities, IRSL and OSL depletion indices and the IRSL: OSL were calculated (Munyikwa et al., 2021). This helped to identify the most suitable intervals/depths for absolute dating. 10-15 g of sediment was collected from each selected position for dating purposes. These samples were subsequently analysed at the luminescence laboratories of the University of St Andrews.

Luminescence ages are calculated as the quotient of the burial dose (in Gy) over the effective environmental dose rate (in mGy a^{-1}). Equivalent dose (De) determinations were made using the single-aliquot regenerative dose (SAR) OSL method (Murray and Wintle, 2000) on sets of 24 aliquots per sample. The burial dose was estimated from the central dose estimate of De values. The dose rates to these samples were determined by quantifying the concentrations of radionuclides U, Th, and K by mass spectrometry, which were converted to effective environmental dose rates, using the conversion factors of Cresswell et al. (2018). Fractional water content values ranged from 11 to 27%. For more detailed information about the OSL procedure and results, see supplementary material S2.

3. Results and interpretation

3.1. Seismic stratigraphy

Seismic interpretation of the 2D high-resolution sub-bottom profiles enabled the identification of seven distinct acoustic units (units A to F, with Unit A being the oldest; Fig. 2A–C, Table 4), defined by their lateral continuity, geometry, thickness variations, internal architecture and acoustic facies. While the stratigraphic framework presented here was established using all mapped units, particular attention is given to Unit C. By correlating its acoustic characteristics with lithological data, the nature and depositional history of this unit are assessed in greater detail.

Unit A is the lowermost unit visible in this study, characterised by very low-amplitude, irregular, and discontinuous internal reflections (Fig. 2A-C). It has a thickness of up to 10 m, thinning northwards. A high-amplitude, irregular, but mostly continuous reflection defines the upper boundary, clearly separating Unit A from the overlying Unit B. However, in the northern part of the area, which is the focus of this study, the base of Unit A is poorly resolved due to reduced acoustic penetration.

Unit B displays a largely transparent acoustic facies with little internal structure, apart from some incoherent, scattered low-amplitude reflections (Fig. 2A-C). Locally, low-amplitude hummocky to mounded geometries are observed. The lower boundary is marked by a sharp, continuous, undulating high-amplitude reflection, which in places becomes discontinuous and hummocky. The upper contact varies spatially. In many areas, Unit B is capped by Unit D or truncated and incised by features associated with Unit E, while in the NW part of the area, it is eroded and overlain by Unit C. Where these overlying units are absent, Unit B is conformably overlain directly by Unit F, separated by a continuous, high-amplitude reflection. Unit B is widespread across the area but shows pronounced thickness variations (2-25 m). Our study focuses on the northern sector, where the unit attains its maximum thickness of 25 m.

Unit C is spatially restricted to the NW part of the study area, covering Unit B, with its base marked by low-amplitude, irregular, discontinuous, hummocky reflections (Fig. 2A-B). It comprises two main subunits: (i) parallel to sub-parallel, moderate-to high-amplitude laminated reflections deposited close to the basal boundary (subunit C1) and (ii) a semi-transparent deposit with generally weak reflectors, occasionally showing patchy, discontinuous, serrated-shaped reflections (subunit C2). The semi-transparent infill (C2) is acoustically similar to Unit B, while the deposit containing laminated reflections (C1) is significantly thinner and occurs only at the base of Unit C. These two subunits are separated from each other by a moderate-to high-amplitude, wavy, continuous reflection. The upper part of Unit C is heavily eroded by Unit E incisions and possibly locally overlain by Unit D. Where Unit E is absent, it is bounded by a high-amplitude continuous

Table 2
Radiocarbon dating results for DB_VC01 core.

Core	Lab code	Depth in core (cm)	Sample type	Conventional radiocarbon date (^{14}C a BP)	Uncertainty (^{14}C a BP)	Calibrated radiocarbon age (cal a BP) (2σ)[a]	IRMS δ13C (‰)
BE2023-19 DB_VC01	Beta-735480	36	Shell *Varicorbula gibba*	1130	30	660 – 448 95.4%	2.8
	Beta-735481	100	Shell *Turritellinella communis*	5080	30	5413 – 5039 95.4%	4.5
	Beta-735482	180	Shell *Cerastoderma edule*	8480	30	9061 – 8685 95.4%	1.8
	Beta-740264	245	Shell *Scrobicularia plana*	8740	30	9400 – 9054 95.4%	−0.26
	Beta-735485	275	Shell *Cerastoderma* cf *edule*	8650	30	9286 – 8968 95.4%	0.5
	Beta-693932	281	Shell *Cerastoderma glaucum*	8770	30	9422 – 9094 95.4%	−1.4

[a] Calibration curves used: Marine20 for shell samples (Heaton et al., 2020).

Table 3
Burial doses, number of aliquots measured, total effective environmental dose rates, and corresponding depositional ages derived from OSL dating of cores south of Dogger Bank. Further details are provided in supplementary material S2.

Core	Lab code	Depth (cm)	Aliquots (n)	Palaeodose (Gy)	Dose rate (mGy a^{-1})	Age (ka)
BE2023-19 DB_VC01	CERSA1774A	320.5	21	16.0 ± 0.4	0.87 ± 0.04	18.45 ± 1.04
BE2023-19 DB_ VC02	CERSA1775A	123.5	18	95.8 ± 3.2	3.17 ± 0.15	30.26 ± 1.74
BE2023-19 DB_VC02	CERSA1775G	269.5	21	92.4 ± 5.0	2.84 ± 0.14	32.49 ± 2.34

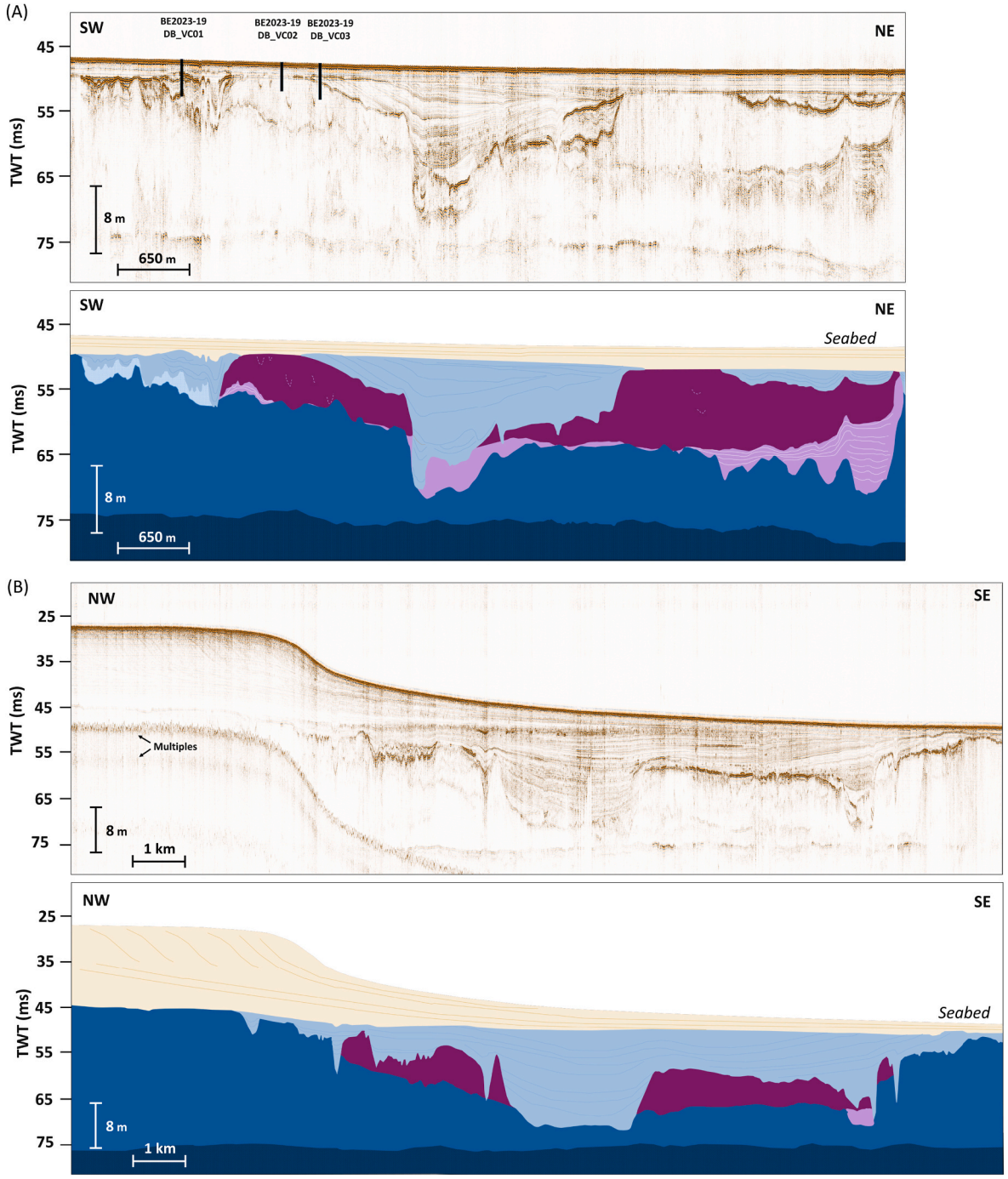


Fig. 2. (A-C) High-resolution sub-bottom profiles showing the main stratigraphic units identified in the study area (see Fig. 1 for locations). Top: uninterpreted acoustic profiles. Bottom: interpreted stratigraphy, with coloured intervals representing the main units assigned to regional formations. Sediment core locations are shown in Fig. 2A (see Fig. 3). (D) 3D reconstruction of the base of the lake unit (base Unit C), illustrating the morphology of the basin (reconstructed in ArcScene). The red lines mark the location of the lake sediments (subunits C1 and C2) on the acoustic sections shown in Fig. 2A and B. Bottom left: 2D illustration of the mapped basin (Unit C), with arrows indicating its length and breadth (lake location shown in Fig. 1).

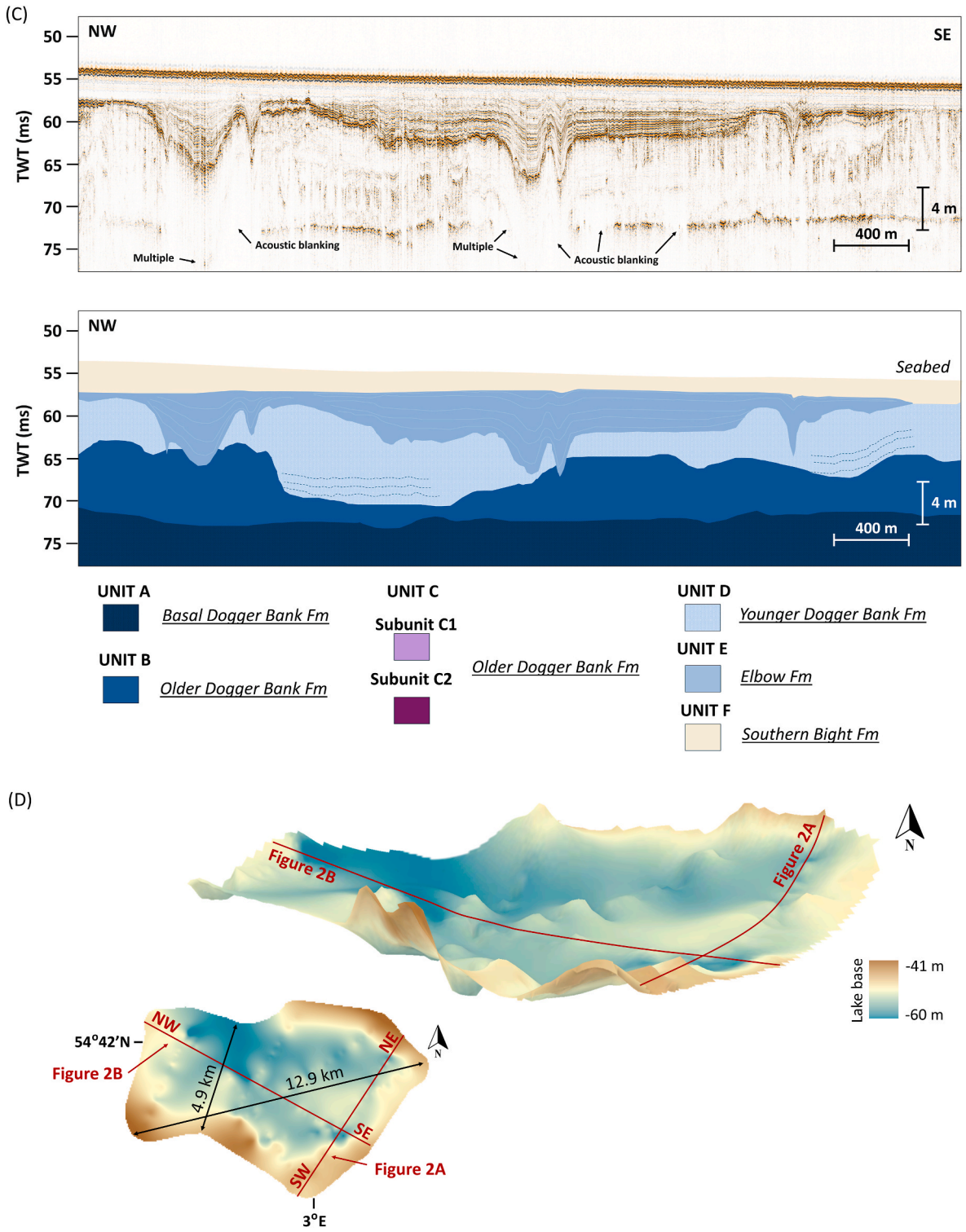


Fig. 2. (*continued*).

reflector (unconformity) separating it from Unit F. Overall, the base of Unit C exhibits a basin-like geometry, while Unit C itself represents its sedimentary infill, reaching a thickness of max. 19 m (Fig. 2D).

Unit D is characterised by medium-to high-amplitude hummocky reflections and overlies Units B and C (Fig. 2A-C). Its basal boundary is expressed as a weakly defined, wavy reflection that locally exhibits a higher amplitude. The base of Unit D lies between ~2.4 and 8.8 m below the seafloor, although its full thickness cannot be reconstructed because its upper part is extensively truncated by incisional features (Unit E). The top of Unit D is either incised by Unit E channels or capped by a high-amplitude reflector marking the transition to Unit F.

Unit E represents multiple erosional incisions of varying sizes and cross-sectional shapes (Fig. 2A-C). Most incisions exhibit incisional depths from 5 to 15 m, with some extending to 25 m. Depending on the spatial occurrence of the underlying units, the erosional features usually truncate units B, C and/or D. High-amplitude and high-frequency, continuous, sub-parallel reflections mark their infill. Toplap terminations are observed at the top of the fill, while onlapping patterns are

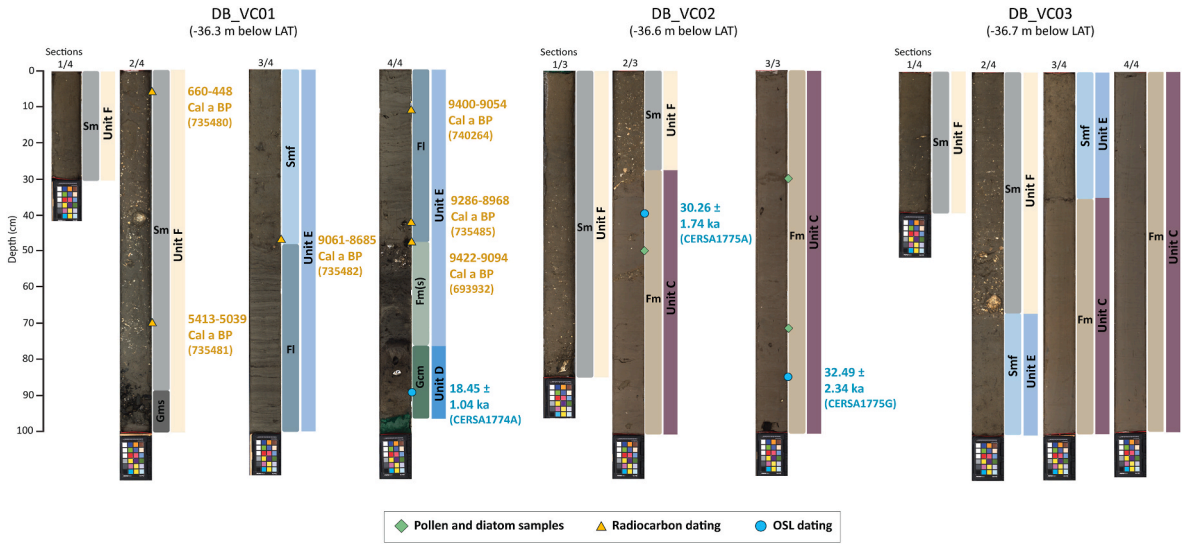


Fig. 3. Photographs of vibrocores DB_VC01, DB_VC02, and DB_VC03 showing the lithofacies and stratigraphic units alongside each section. Core locations are shown in Figs. 1 and 2A and summarised in Table 1. Positions of samples for pollen and diatom analysis and dating (radiocarbon and OSL) are marked along the cores (see Tables 2 and 3).

Table 4
Regional formations and stratigraphic units identified within the study area, with associated observed acoustic facies, compiled from Cameron et al. (1992), Cotterill et al. (2017a,b), Phillips et al. (2018), Rijsdijk et al. (2005) and Stoker et al. (2011).

Era	Age	Formations	Subdivisions Cotterill et al. 2017a,b	Environment	Units (this study)	Reflection description (this study)
Holocene	MIS 1	Southern Bight Fm		Marine	F	Parallel, low amplitude, moderate frequency, continuous.
		Elbow Fm (UK) ---------- Nieuwkoop Fm/ Naaldwijk Fm (NL)		Estuarine, brackish, intertidal	E	Sub-parallel, high amplitude, high frequency. Channels fill.
Weichselian/ Devensian	MIS 2	Twente Fm (UK) ---------- Boxtel Fm (NL)		Periglacial aeolian	Absent	Not observed in the acoustic profiles.
		Botney Cut Fm (UK) ---------- Dogger Bight Fm (Botney Cut member) (NL)		Subglacial, glaciolacustrine, glaciomarine	Absent	Not observed in the acoustic profiles.
	MIS 5d?-2	Bolders Bank Fm (UK) ---------- Dogger Bight Fm (Bolders Bank member) (NL)		Subglacial (till)	Absent	Not observed in the acoustic profiles.
	MIS 5d?-2	Dogger Bank Fm (UK) ----------	Younger Dogger Bank Fm	Glacial, periglacial, aeolian transitions	D	Medium to high amplitude hummocky reflections.
		Dogger Bight Fm - Dogger Bank Member (NL)	Older Dogger Bank Fm	Glacial	C	Transparent and mostly structureless. Low-amplitude, asymmetric, patchy, and sporadic reflections (C2). Sub-parallel, high amplitude and high frequency, continuous to discontinuous reflections often at the base of the basin (C1).
					B	Mostly massive, transparent, structureless. Very-low amplitude asymmetric reflections.
			Basal Dogger Bank Fm	Periglacial and aeolian	A	Structureless, semi-transparent.

frequently noted at the incision margins. A high-amplitude wavy reflection marks the basal boundary, and a high-amplitude, mostly flat reflection marks the top. The incision infills of Unit E are directly covered by the younger deposits of Unit F.

Unit F represents the stratigraphically youngest seismic unit, directly overlying all previous units, except Unit A, throughout the study area (Fig. 2A-C). It is primarily characterised by continuous, parallel, low-amplitude and moderate-frequency reflections. Its upper boundary is marked by a high-amplitude reflection, which corresponds to the present-day seafloor, while its base corresponds to a planar reflection (unconformity). Its thickness is highly variable, ranging from 1 to 19 m, with the maximum thickness reached in the north of the study area.

Correlation with regional formations

The acoustic-stratigraphic framework established in this study can be

correlated with previously defined formations within the Dogger Bank region (Table 4) (Cameron et al., 1992; Cotterill et al., 2017a,b; Stoker et al., 2011). Based on acoustic facies characteristics, reflection geometries, and stratigraphic position, Units A-D are interpreted to correspond to subdivisions of the Weichselian-age Dogger Bank Formation (DBF), deposited in glacial and periglacial settings. Following the classification proposed by Cotterill et al. (2017a,b) and comparison with published seismic datasets (Andresen et al., 2022; Phillips et al., 2018; Roberts et al., 2018), Unit A is assigned to the Basal DBF, Units B and C to the Older DBF, and Unit D to the Younger DBF. Unit E, assigned to the Elbow Formation, represents Late Weichselian-Holocene channel systems and marks the Holocene transgression, whereas Unit F comprises marine sediments of the Southern Bight Formation (Cameron et al., 1992; Roberts et al., 2018; Stoker et al., 2011).

3.2. Cores sedimentary facies and dating

Seven lithofacies were identified in the DB_VC01, DB_VC02 and DB_VC03 vibrocores. These lithofacies are described in detail below, and images and lithofacies successions are shown in Fig. 3.

Fm - massive silt with dropstones

Massive, stiff, reddish-brown silt with embedded clasts and chalk fragments. Microcharcoal is also present, while the deposit is barren of foraminifera and shells. Clasts are small to large pebbles (<1.5 cm), subrounded to sub-angular in shape. The clasts, interpreted as dropstones, are abundant and scattered throughout the fine-grained matrix. Sorting is poor, without a clear stratification or internal sedimentary structure. Isolated sand pockets are locally visible. Clear signs of bioturbation are present in the upper part of this unit (e.g., between 182 and 128 cm in DB_VC02 core), which appear as a sandy layer with shell fragments, similar to lithofacies *Sm*.

Gcm - coarse sand with pebbles

Poorly sorted fine to coarse brownish-grey sand with numerous clasts. Sub-angular granules and pebbles of up to 3 cm diameter occur within the sandy mica-rich matrix, together with fragments of plant material.

Fm(s) - clay with shell hash

Dark grey, clay-rich matrix with shells and shell fragments, with rare pebble-sized clasts. The fine-grained matrix consists primarily of clay and silt, with plant material. Shell and shell-fragment concentrations increase markedly towards the upper boundary.

Fl - laminated silts and clays

Grey clay and darker grey silts in alternating thin laminas. The silts are organic-rich and appear in wavy parallel laminae, while small shells and shell fragments are found within the silt laminae. The clay laminae become thicker towards the base.

Smf - fine sand with granules

Fine grey sand with black granules, moderately shorted. A small assemblage of dispersed shell fragments is present, and some plant material. The shape of granules ranges from sub-angular to rounded.

Gms - gravel supported matrix

Clast-supported layer of varied lithologies and colours, and scattered shell fragments. The matrix ranges from granules to medium pebbles (up to 3 cm). This deposit is very poorly sorted, with angular to subrounded shapes and coarse sand.

Sm - massive sand with shells and shell fragments

Massive, brown to dark-brown, well-sorted sand with abundant shell fragments and complete shells, present at the top of all cores. This facies lies immediately below the seafloor and contains shell material of variable sizes (up to 6 cm) distributed throughout. Shell content increases towards both the upper and lower boundaries, with a distinct shell hash layer developed towards the base.

Core DB_VC01 was recovered from a channel feature within acoustic Units D, E and F and comprises six main sedimentary units (Figs. 2 and 3). The basal sandy unit with clasts (facies *Gcm*; 328-307 cm) yielded an OSL age of 18.45 ± 1.04 ka (CERSA1774A, Table 3) and is assigned to Unit D. It is sharply overlain by a clay-rich unit (facies *Fm(s)*; 307-281 cm) containing organic debris and shell fragments, with its upper boundary dated by radiocarbon to ca. 9422-9094 cal a BP (Table 2). Facies *Fm(s)* contains mollusc specimens of *Scrobicularia plana, Cerastoderma indet.*, *Peringia ulvae*, *Littorina saxatilis tenebrosa*, and *Mytilus edulis*. Above this, interlaminated clay silts with organic material and shells (facies *Fl*; 281-180 cm), bounded by sharp basal and upper contacts, yielded radiocarbon ages of ca. 9286-8968 cal a BP at the base and ca. 9061-8685 cal a BP at the top (Table 2). A fine sand layer (facies *Smf*; 180-128 cm) with shell fragments and granules forms a distinct boundary with an overlying pebble-hash layer (facies *Gms*; 128-112/120 cm). Within facies *Fl* and *Smf*, *in situ* faunal assemblages are dominated by *Cerastoderma glaucum*, *Rissoa membranacea*, *Peringia ulvae* and *Ostrea edulis*. Unit E channels record lithological changes with multiple depositional phases represented by facies *Fm(s)*, *Fl*, and *Smf*. The pebble-hash layer, in turn, sharply separates the underlying sand from the uppermost shelly sands (facies *Sm*; 112/120-0 cm). Facies *Sm* mainly consists of *in situ* specimens, represented by *Varicorbula gibba, Chamelea striatula* and *Thyasira flexuosa*. The shelly sands above the pebble-hash, corresponding to Unit F, are dated to the Middle to Late Holocene.

Core DB_VC02 was obtained through Units C and F and contains two sedimentary units. The lower part of the core consists of massive silts containing numerous clasts up to pebble size (facies *Fm*; 284-117/114 cm), assigned to Unit C (subunit C2). This unit is barren of shells and foraminifera. Its nature is investigated in more detail in the following subsections. Localised bioturbated layers with thin shelly sand intervals and sand pockets occur sporadically within the silt matrix between ~125 and 185 cm. OSL ages were obtained for two samples from this unit. The lower OSL sample at 269.5 cm yielded an age of 32.49 ± 2.34 ka (CERSA1775G), while the upper sample at 123.5 cm suggested an OSL age of 30.26 ± 1.74 ka (CERSA1775A, Table 3). The upper part of the core comprises shelly sands (facies *Sm*; 117/114-0 cm), similar to those observed in core DB_VC01 and assigned to Unit F. It sharply and erosively overlies the massive silts of Unit C. As both OSL samples were collected from the upper part of Unit C (Fig. 2A), these results indicate that deposition of the massive silts occurred prior to and during ca. 32.5-30.3 ka.

Core DB_VC03, which penetrates Units C, E and F, comprises three main sedimentary units. The lower part of the core consists of stiff silts with dispersed clasts (facies *Fm*; 341-175 cm), lithologically comparable to Unit C in DB_VC02. This is sharply overlain by a fine sandy layer containing shell fragments (facies *Smf*; 175-105 cm), representing the channel infill facies of Unit E, also observed in DB_VC01. The uppermost unit comprises shelly sands (facies *Sm*; 105-0 cm) assigned to Unit F, equivalent to the surface deposits encountered in both DB_VC01 and DB_VC02. Although undated, the stratigraphic relationships and lithological similarities suggest that DB_VC03 preserves the same depositional succession as inferred for adjacent cores.

3.3. CT scan segmentation of clasts

A detailed segmentation analysis was performed on the CT-scanned images of the massive silt unit with the pebble-sized clasts (i.e. lower section of core DB_VC02, lithofacies *Fm*, Unit C). The segmentation confirms the presence of numerous discrete clasts dispersed within the homogeneous silt unit and allowed the extraction of all voxels corresponding to these clasts. Identified clasts had an equivalent spherical diameter (ESD) of 0.28 mm or greater, with 0.28 mm representing the

smallest clast size observed in this dataset. The resulting dataset, shown in Fig. 4, illustrates the scattered distribution and isolated nature of all the clasts within the scanned volume. An example of sand-sized particles identified within the mud matrix is illustrated in Fig. 5A. For the subsequent morphometric characterisation of each voxel, only clasts with ESD values exceeding 2 mm were considered.

A total of 423 coarser clasts were identified and segmented from the 1 m split section 3/3, all larger than 2 mm (granule to pebble size). The clasts are represented as isolated, scattered voxels, distributed randomly within the fine-grained deposit, without indication of vertical clustering, zonation or notable changes in abundance. Particle size distribution based on ESD and Feret diameters shows a right-skewed pattern, with the majority falling within the granule size range (ESD 2-4 mm) and a smaller fraction (~11%) corresponding to pebble-sized grains (ESD >4 mm) (Fig. 6A and B). Based on aspect ratio, clast shapes are classified into four subgroups, ranging from equant to flattened forms. The histogram in Fig. 6C shows that most clasts exhibit sub-equant to elongated geometries (AR = 0.3-0.8). Extremely flattened or platy particles (AR < 0.3) are rare within the population, while only a few particles display equant morphologies (AR > 0.8). A moderate positive correlation ($R^2 = 0.49$) exists between sphericity and aspect ratio, such that clasts with moderate to high sphericity generally reflect sub-equant to equant shapes, consistent with the expectation that near-equant clasts are more spherical (Fig. 6D). Clast orientation spans the full range of measured angles, with no single preferred orientation class dominating the population. The voxels are broadly distributed and lack a directional maximum, indicating predominantly random orientation throughout the scanned volume (R = 0.165; Fig. 6E).

Clast morphologies

Selected pebbles were extracted from the cores DB_VC02 and DB_VC03 and examined macroscopically to assess their surface textures and morphology (Fig. 5B and C). CT segmentation and visual inspection confirm a wide range of clast morphologies, from subrounded to angular shapes, including specimens with sharp or irregular edges. Once extracted from the matrix, it becomes apparent that the clasts display a diverse range of colours, including grey, reddish-brown, light brown, and white, reflecting a heterogeneous lithology (Fig. 6B). All analysed samples are sedimentary and low-grade metasedimentary rocks, predominantly sandstone, limestone (commonly chalk), shale, and occasionally charcoal (S. Dewaele, personal communication). No foliation, high-grade metamorphic minerals, or evidence of high-temperature or high-pressure alteration was observed. Sandstone clasts are dominated by quartz, while the limestone and shale clasts exhibit their characteristic fine-grained textures. No feldspar or mica was identified, while the apparent reflective surfaces are attributed to quartz rather than accessory minerals. Most clasts exhibit rough, irregular surfaces, with partially abraded or fractured faces. Several specimens exhibit distinct grooves, pits, and facets, and some possess broken or platy edges (Fig. 5C), typical of glacially eroded or ice-transported material (Benn and Evans, 2010; Bozzano et al., 2021).

The combination of their morphological and textural characteristics, varied lithologies, and occurrence within a massive, homogeneous silt matrix (Bennett et al., 1996; Conolly and Ewing, 1965; Shipboard Scientific Party et al., 1995) leads us to interpret these clasts as dropstones deposited in a glacially influenced environment.

3.4. XRF core scanning

XRF scanning of core DB_VC02 reveals a distinct compositional change that occurs abruptly at 112-118 cm, where all major element signals shift simultaneously, defining a sharp geochemical boundary (Fig. 7). This transition coincides with the lithological contact between the massive, stiff silts (facies *Fm*; Unit C, subunit C2) and the overlying shelly marine sands (facies *Sm*; Unit F).

Sr and the log (Si/Ti) display similar patterns, with low values throughout the silt unit (lower part of the core, up to 115 cm), followed by a sharp increase and elevated values above the boundary with the overlying sand interval (approximately 85-115 cm). The log (Si/Ti) is an indicator of biogenic silica and productivity, with higher values indicating increased biogenic input (Adamson et al., 2019; Davies et al., 2015; Gjerde et al., 2018). Sr is typically enriched in marine settings and associated with biogenic carbonates such as shells, providing a reliable proxy for marine influence (McCloskey et al., 2018; Ramírez-Herrera et al., 2012; Small et al., 2025). Two localised spikes in the log (Si/Ti) at 170-175 cm and ~140-143 cm correspond precisely to bioturbation structures (grey shaded bands, Fig. 7). These structures are interpreted as burrows infilled with marine sands and shell fragments typical of the overlying unit, which explains the local increases. Ti, K, and Fe also clearly separate the core into two geochemically discrete groups, supporting that these sedimentary units have different compositional signatures. Ti, K, and Fe signals are higher in the lower silt interval but decrease markedly within the upper sandy facies, displaying broadly similar variability and depth trends. Ti, K, and Fe are commonly used as proxies for terrigenous input, reflecting the contribution of detrital material (Blanchet et al., 2009; Carlson et al., 2008; Kylander et al., 2011; Martin-Puertas et al., 2017; Tjallingii et al., 2010). The bioturbation levels described above are also evident as abrupt drops in the Fe and Ti records, with coeval but more subdued declines in the K record, indicating reworked marine pockets (grey shaded bands, Fig. 7). The enrichment of Ti, K, and Fe within the lower silts is consistent with uniform fine-grained, terrigenous sedimentation.

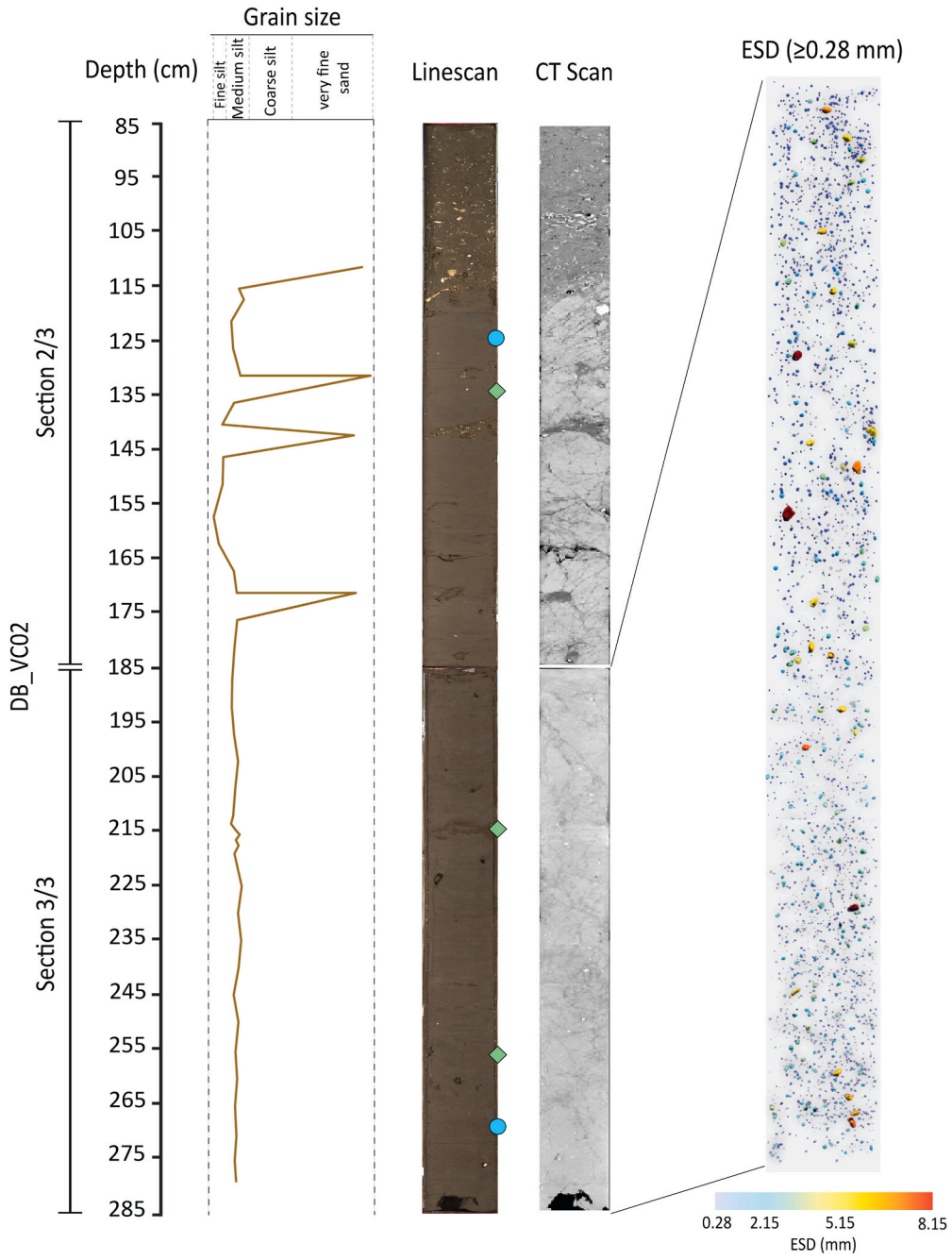
Similar patterns are observed in log (Rb/Sr), a geochemical proxy for weathering, where higher ratios reflect increased input of terrigenous detritus, and lower ratios indicate a greater contribution from chemical/biogenic deposits (Jin et al., 2001; Xu et al., 2010).

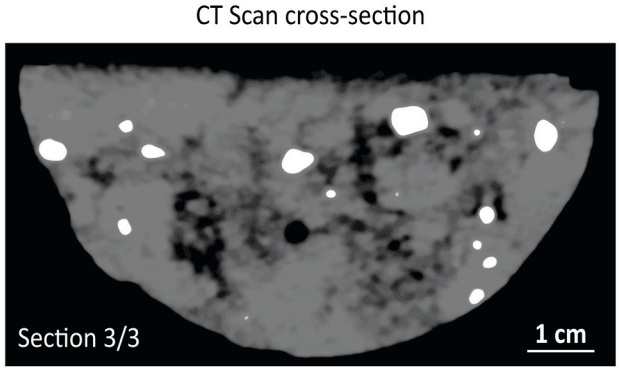
The significant geochemical shift between these sedimentary units indicates a change in depositional environment. Combined, the geochemical proxies suggest that the lower stiff silts of Unit C were deposited in a terrigenous-dominated environment with little to no marine influence, while the overlying sands of Unit F are clearly marine in origin.

3.5. Diatom and pollen analysis

Diatoms were almost entirely absent from the DB_VC02 core, with only a small assemblage recovered from the lower part of the sequence (sample at 213.5 cm). This assemblage comprised four isolated frustules, mostly fragmented, including *Amphora ovalis var. libyca, Cocconeis sp., Eunotia sp.,* and *Ulnaria sp.* Those encountered are often associated with freshwater conditions, with the majority being epiphytic in habit. Overall, the diatom record is characterised by extremely low abundance, low diversity, and poor preservation.

In the same core (Unit C), pollen was present (Fig. 8A). The assemblage was dominated by *Pinus* (>40% TLP). Other taxa present included *Poaceae*, *Picea*, *Betula* and *Alnus*, with *Corylus avellana*-type in lower proportions. Pre-Quaternary spores were also abundant (20% TLP + TPQ), indicating the incorporation of reworked material. Reworked material is also indicated by the presence of *Carya* and *Pterocarya*, usually restricted to Early Pleistocene or older deposits, which is also likely applicable to the *Taxiduaceae*, along with *Ostrya carpinifolia*-type, usually found in Middle Pleistocene or older deposits. Although the reworked component is prevalent within the sequence, the presence of taxa including *Empetrum nigrum*, *Helianthemum*, *Saxifrage granulata*-type and *Lycopodium clavatum* are all indicative of colder environments, with *Stellaria holostea* and *Geum* possibly indicative of marsh or an exposed upland environment. Heath communities are inferred by the presence of *Vaccinium*-type and *Calluna vulgaris*, while *Bryophyta* indicate mosses. The freshwater algae *Pediastrum* occurs in low levels, indicative of a freshwater source. These taxa may therefore be representative of local vegetation.





(caption on next page)

Fig. 4. (Top) Grain-size results for core DB_VC02 (sections 2/3 and 3/3), with core photographs and CT-scanned images. Particles larger than 0.28 mm ESD (approximately the sand fraction and above) are colour-coded by size, indicating their abundance and distribution throughout section 3/3. (Bottom) CT slice (at 237 cm) from section 3/3, illustrating the spatial presence of numerous outsized clasts (shown in white) within a silt-dominated sediment matrix. Pollen and diatom sample locations are shown by green symbols, and OSL locations by blue symbols.

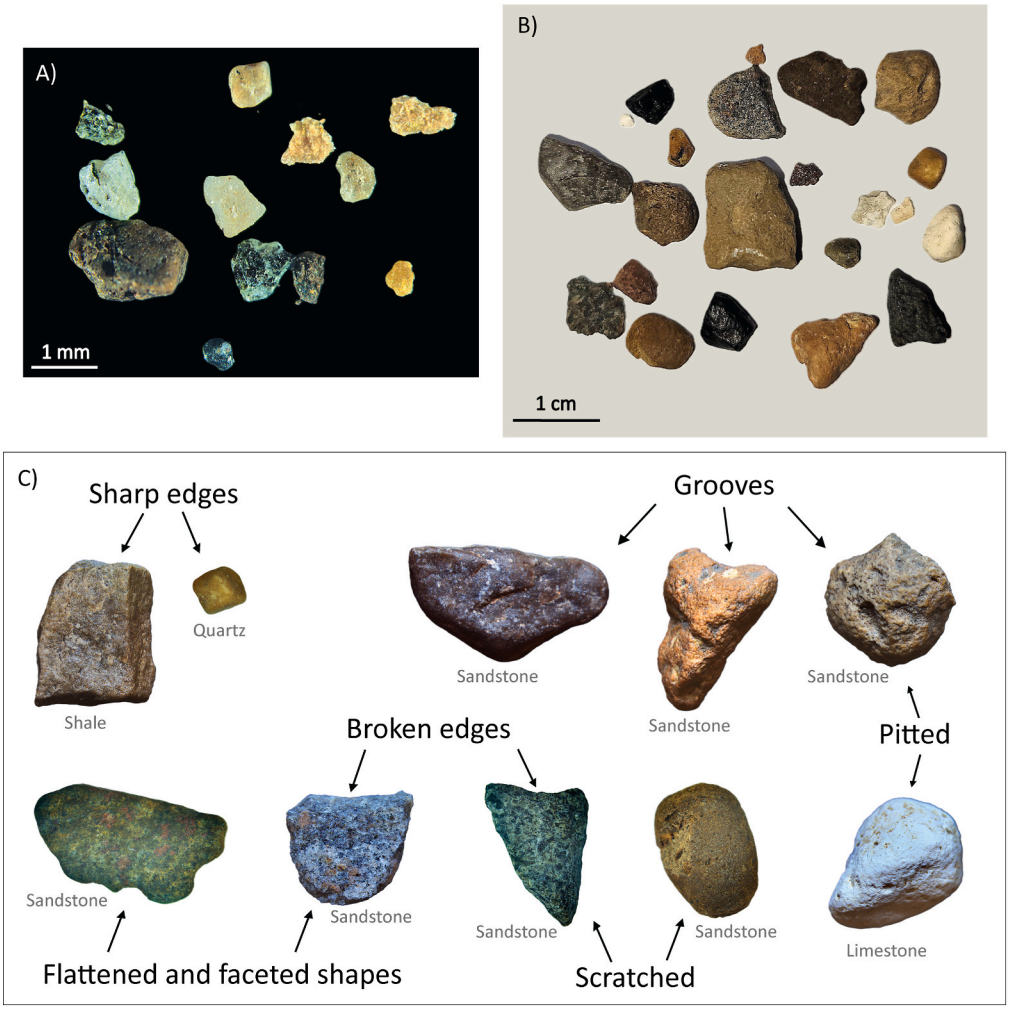


Fig. 5. Selected dropstones extracted from cores DB_VC02 and DB_VC03, illustrating their varying morphology. (A) Microscopic illustration of sand-sized clasts from DB_VC02. (B) Granules and pebbles from both cores showing subangular to subrounded shapes, a wide range of morphologies, and diverse lithologies. (C) Macroscopic samples from panel B exhibit glacially influenced features, including grooves, faceted and flattened shapes, and sharp or broken edges.

4. Discussion

4.1. Sedimentological evidence for a glaciolacustrine setting

Grain size and clast analyses

The coarser grains and clasts identified within stratigraphic Unit C (subunit C2) in cores DB_VC02 and DB_VC03 are interpreted as ice-rafted debris (IRD), with individual outsized clasts representing dropstones, providing direct evidence of past glacial influence in the study area. Random orientations, absence of imbrication, and lack of current- or flow-induced alignment indicate vertical deposition through the water column before incorporation into a settled fine sediment matrix, supporting this interpretation (Carrivick and Tweed, 2013). Dropstones are widely recognised as indicators of glacially influenced environments (Bozzano et al., 2021) and are diagnostic of glaciolacustrine or glaciomarine settings (Carrivick and Tweed, 2013). Defined as single, exotic clasts of anomalous size and lithology relative to the host matrix, they are deposited by ice rafting from icebergs or seasonal ice floes into fine-grained, massive sediments (Arnaud and Martini, 2009; Bennett et al., 1996; Carrivick and Tweed, 2013).

Chronology

The OSL ages obtained from core DB_VC02, with the lower part yielding an age of 32.49 ± 2.34 ka (269.5 cm) and the upper part 30.26 ± 1.74 ka (123.5 cm), indicate that subunit C2 is stratigraphically consistent, with increasing age with depth. The samples were assessed as well-bleached, and the resulting ages are therefore considered reliable. Although the limited number of dated samples does not allow precise determination of sedimentation rates, the overlap between the two ages within their respective uncertainties suggests broadly continuous sedimentation within the basin rather than discrete depositional events. The small age difference, together with the overlapping uncertainties, indicates that deposition of the stiff, fine-grained glaciolacustrine sediments occurred over a relatively constrained interval during late MIS 3. This implies sustained ice-proximal lacustrine conditions, consistent with a prolonged proximity of a Weichselian ice margin.

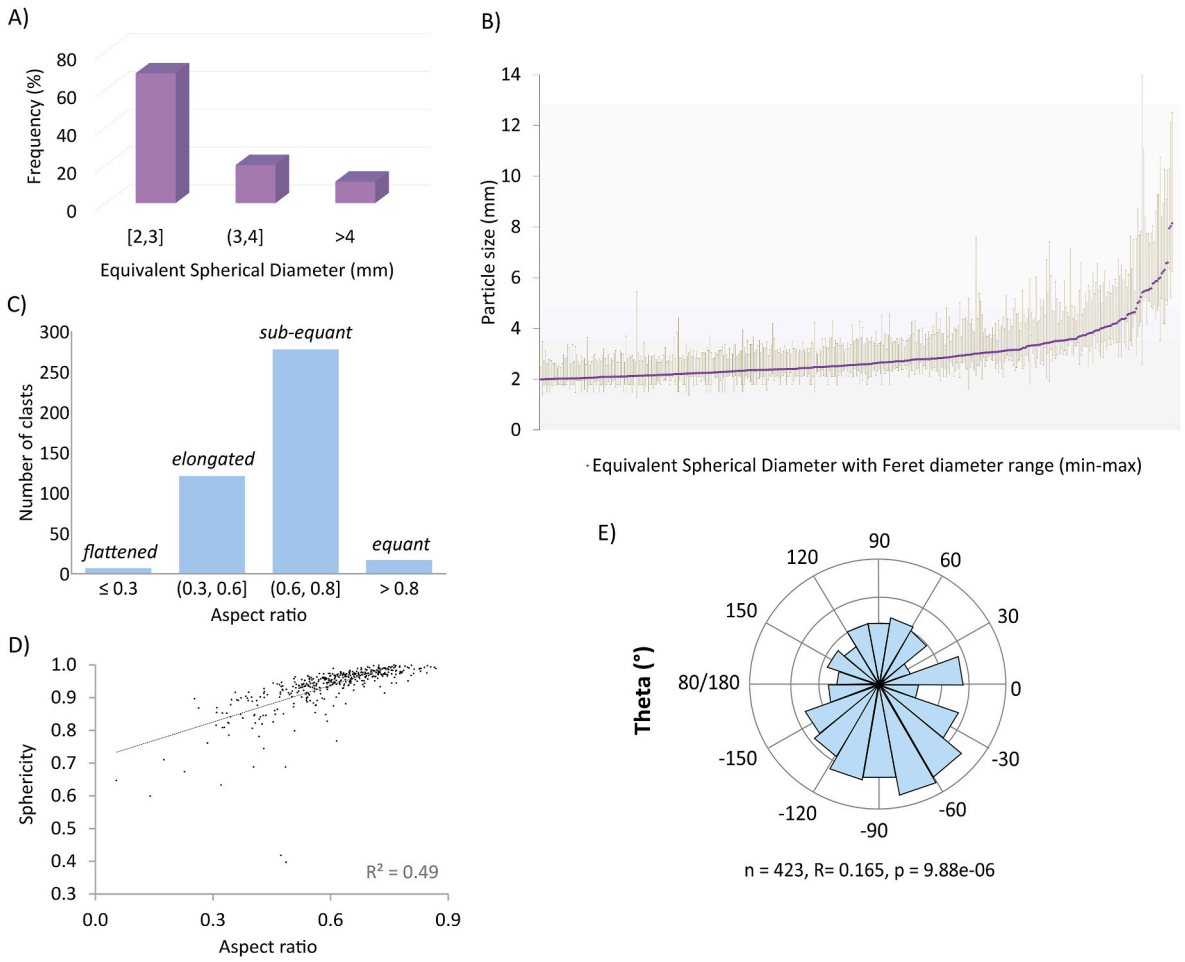


Fig. 6. Analysis of the clasts extracted from the DB_VC02 core (section 3/3). (A) Histogram of Equivalent Spherical Diameter (mm) for clasts classified into three main categories (granules to pebble size) showing frequency per category. (B) Equivalent Spherical Diameter and minimum/maximum Feret diameter for each clast. (C) Aspect ratio histogram grouped into four categories, showing the number of clasts in each group. (D) Scatter plot of sphericity versus aspect ratio. (E) Rose diagram showing the orientation of clasts, produced in RStudio (n = number of clasts, Rayleigh (R) = orientation parameter, p = significance value).

Geochemistry

Sr concentrations in subunit C2 are extremely low. As Sr occurs in much higher concentrations in seawater than in freshwater (López-Buendíı;a et al., 1999; Ramirez-Herrera et al., 2007, 2012), the absence of an enhanced Sr signal in subunit C2 demonstrates that these sediments exhibit no geochemical imprint of marine influence. This is in clear contrast to the markedly higher Sr values in the shelly sands of Unit F, which may instead reflect a freshwater interpretation. If so, the overlying erosive contact could represent a subsequent marine transgression, marking a rapid environmental shift. Hence, this pattern does not provide support for a glaciomarine depositional setting for subunit C2 but favours glaciolacustrine conditions. Elevated concentrations of both Ti and Fe, such as those detected in subunit C2, have also been associated with enhanced glacially derived (i.e. detrital) sediment influx in proglacial lakes in other studies (Adamson et al., 2019). Ti in particular is a robust indicator of glacial influence, reflecting the meltwater-driven input of glacially derived detrital material into lake sediments (Bakke et al., 2009; de Wet et al., 2018). Lake sediments showing high Ti coupled with low biogenic silica (log (Si/Ti)) are interpreted as reflecting colder temperatures associated with glacial influence (Stansell et al., 2010), a pattern that is also evident in subunit C2. Such periods of cooler climatic conditions in lake sediments are also reflected by higher log (Rb/Sr), as these are known to record a sensitivity to temperature fluctuations (Fritz et al., 2018). Increased Ti, K, and Fe in subunit C2 mirror similar elemental shifts documented in proglacial lakes and are associated with phases of glacier advance (Stansell et al., 2013). Taken together, the lack of a strong marine geochemical signal, coupled with the multi-element detrital signature, indicates that a glaciolacustrine depositional environment is the most plausible interpretation of the sediments associated with subunit C2.

Microfossil analyses

The diatom assemblage reveals very low abundances and only isolated occurrences of diatoms in subunit C2, which, together with their fragmented appearance and poor preservation, could indicate reworking and subsequent transportation of isolated frustules into the depositional environment. That said, a freshwater signal might be reflected by the presence of *Amphora ovalis* var. *libyca,* a freshwater diatom often associated with epipelic (muddy) conditions, together with diatom genera of *Cocconeis sp., Eunotia sp. and Ulnaria sp.,* which are usually linked to freshwater or vegetated settings (Vos and de Wolf, 1993). The restricted diatom level within this unit is also reflected by the low log (Si/Ti) values, which illustrate low production of biogenic silica (Balascio et al., 2011; Melles et al., 2012). Similar limited biological activity with low log (Si/Ti) has been recorded elsewhere in paleo-proglacial lake environments during glacial depositional phases (Adamson et al., 2019), linked to increased fine-grained sediment input and reduced light penetration (Slemmons et al., 2017).

The palynology record reflects subunit C2 to be a complex deposit, containing a notable proportion of reworked pollen grains, as well as some contemporary pollen. The OSL dating of subunit C2 permits a comparison of the pollen assemblage to possible contemporary

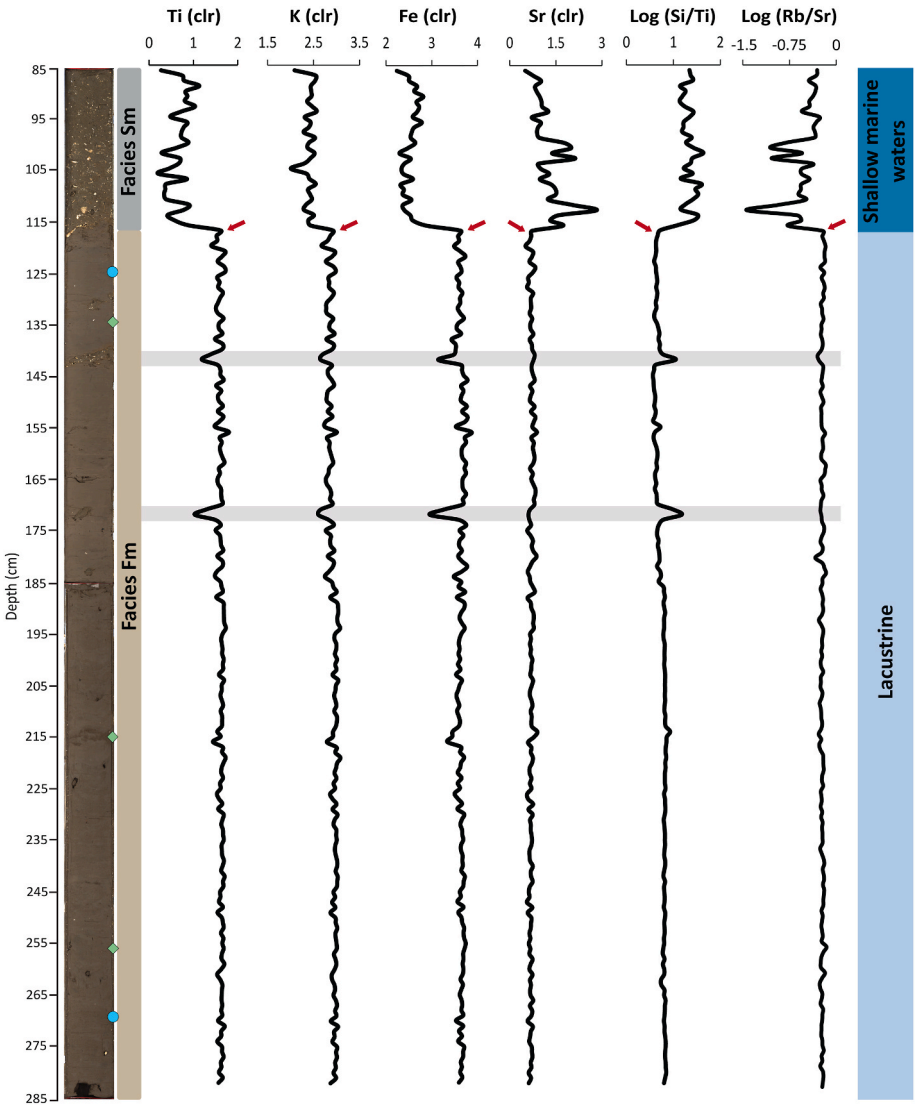


Fig. 7. XRF data for core DB_VC02 (sections 2/3 & 3/3). Lithofacies and interpreted depositional environments are shown alongside the geochemical profiles (Facies Sm = Unit F; Fm = Unit C, subunit C2). Grey zones mark bioturbated layers, whereas red arrows denote the sharp shift in elemental composition reflecting a change in the depositional environment. Pollen and diatom samples are indicated in green, and OSL samples in blue.

sequences within the wider region. The dating is broadly contemporary with two known interstadials within northwest Europe - the Hengelo interstadial (ca. 40-39 ka) and the Denekamp interstadial (ca. 35-32 ka) (Fig. 8B). The pollen record associated with these interstadials is best represented by the Hengelo K.N.Z site and Grouw pollen records (Kasse et al., 1995; Zagwijn, 1961) and, further afield, the La Grande Pile sequence from NE France (Pons et al., 1990; Woillard, 1978), where the Denekamp interstadial has been correlated to the Grande Bois and the Hengelo interstadial to the Charbon Stages. Within the Dutch sequences, the Hengelo interstadial is dominated by non-arboreal taxa, notably *Ranunculus*, Poaceae and Cyperaceae, with *Pinus* less than 10% TLP and *Betula* less than 20% TLP, though an over-abundance of *Pinus* is observed in the base of the Hengelo L.G.M. site sequence (Zagwijn, 1974), where a peak in Cupressaceae is also recorded, consistent with the presence of reworked sediment. Within the La Grande Pile sequence, the Denekamp interstadial is characterised by higher *Pinus*, whereas the Hengelo interstadial has higher *Betula*, a pattern also observed in the sequence from Horoszki Duże in eastern Poland (Granoszewski, 2003). Within the DB_VC02 sequence, *Pinus* exceeds 40% TLP. The fact that many other pollen taxa suggest a high degree of reworking in this sequence might explain the higher than expected presence of *Pinus*. *Betula* contributes 6-10% TLP., which is consistent with the Hengelo interstadial, and the size of some *Betula* pollen grains falls within the range characteristic of *Betula nana* (dwarf birch). Crucially, many of the non-arboreal taxa identified here are considered to be consistent with an MIS 3 environment. Biostratigraphic correlation to either the Hengelo or Denekamp interstadial is challenging, though the latter appears to provide a better match based on the higher *Pinus* component coupled with the presence of a number of other taxa and OSL dating. Overall, the fact that this unit contains a significantly reworked pollen component, combined with the co-occurrence of pollen taxa associated with freshwater and cold climate communities, aligns with our suggested interpretation of a glaciolacustrine environment during MIS 3 in the study area.

Depositional setting

Based on sedimentological, geochemical and microfossil evidence, subunit C2 is interpreted as an ice-proximal lacustrine deposit (Hambrey, 1994; Mager and Fitzsimons, 2007; Nesje et al., 2007; Reitner, 2007). In glaciolacustrine environments, dropstones may be emplaced by several mechanisms of ice rafting, including icebergs calved from an active glacier margin, as well as floating lake ice or river ice (Ashley, 1988, 1995; Carrivick and Tweed, 2013). Mass-flow

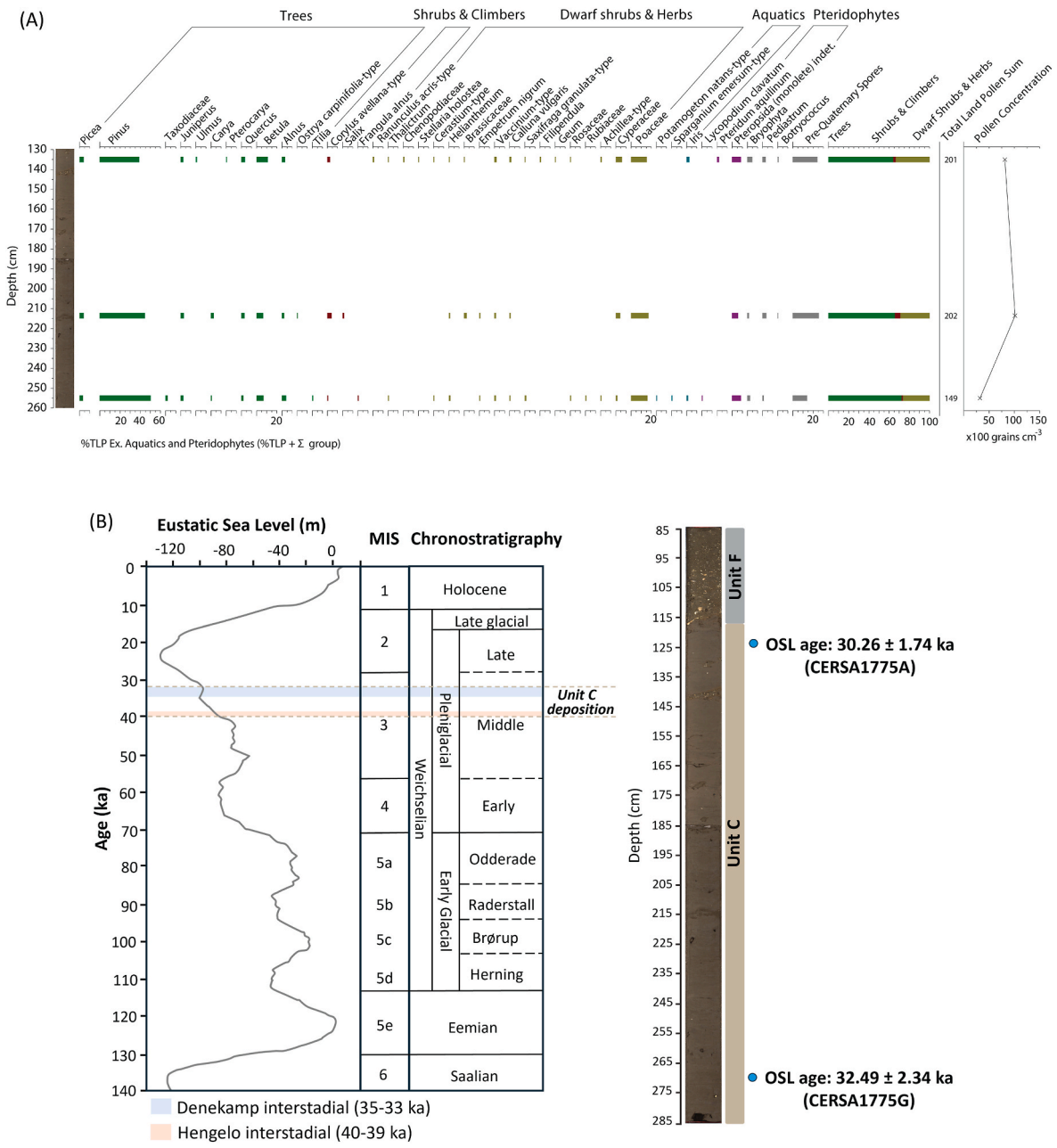


Fig. 8. (A) Pollen assessment results from three samples in core DB_VC02. (B) Synopsis of global eustatic sea-level changes for MIS 6-1 (Lisiecki and Raymo, 2005; Spratt and Lisiecki, 2016) with Hengelo and Denekamp interstadials positioned along the timeline (Van der Hammen et al., 1967; Ran, 1990; Vandenberghe and van der Plicht, 2016). Based on OSL ages and pollen analysis, Unit C is inferred to be deposited during regional Hengelo and/or Denekamp interstadials and sea-level fluctuations during the Middle Pleniglacial (MIS 3).

processes, such as debris flows and turbidites, can also introduce glacial debris into lacustrine sediments (Ashley, 1995; Fulton and Pullen, 1969), but this mechanism is considered unlikely for subunit C2 due to the absence of diagnostic sedimentary structures (e.g., grading, erosional bases). Both iceberg rafting and rafting by floating lake or river ice remain plausible mechanisms for the dropstone deposition. However, debris transported by seasonal lake or river ice typically undergoes some degree of fluvial transport prior to entrainment and therefore tends to consist of more rounded clasts (Sutherland et al., 2022). In contrast, the dropstones in subunit C2 are polymictic, angular to subangular, and commonly display rough surfaces and local faceting, lacking preferential orientation. These characteristics are indicative of debris produced by direct glacial erosion and subsequently released during iceberg melting (Bennett et al., 1996; Martini et al., 2011). Their abundance, lithological diversity and overall angularity further support deposition in a glacio-lacustrine setting proximal to a glacier front, with deposition promoted by iceberg calving, in line with observations from other ice-contact lakes (Aquino et al., 2014; Sutherland et al., 2019, 2022). Although seasonal lake or river ice can transport coarse debris, these mechanisms are less consistent with the observed dropstone morphology in subunit C2. Therefore, the dropstones are most likely interpreted as ice-rafted debris deposited adjacent to a calving ice margin.

In addition to the dropstones, subunit C2 records suspension settling of fine-grained sediments (massive silts) typical of glaciolacustrine environments in which meltwater delivers high suspended-sediment loads and enhances sedimentation rates (Ashley, 1988; Carrivick and Tweed, 2013). According to the lake types defined by Ashley (1995, 1988), C2 most closely resembles river-fed lakes, characterised by massive

fine-grained deposits and low-energy, ice-proximal settings and ice-cliff margin lakes marked by abundant dropstones interbedded with lacustrine mud. Although subunit C2 shares characteristics with river-fed lakes, no fluvial channels or river systems are identified in the available sub-bottom profiling data. However, this does not preclude meltwater entering the lake through diffuse or poorly preserved drainage pathways. That said, the fine-grained deposits are more consistent with sedimentation driven by direct meltwater input from a nearby glacier margin. Together with the abundant ice-rafted debris, these observations indicate that, based on the dataset presented here, subunit C2 was deposited by meltwater-fed suspension settling within a dynamic ice-marginal lake influenced by iceberg calving (Fig. 9). Underflow circulation in ice-contact lakes commonly produces rhythmically laminated lake-floor deposits (Ashley, 1995; Carrivick and Tweed, 2013; Smith and Ashley, 1985). Such conditions could have prevailed during the deposition of subunit C1, as this is consistent with its acoustic character and suggests deposition in a lacustrine bottom environment (Ashley, 1988). Yet the absence of sedimentological data for subunit C1 impedes a more conclusive interpretation (Fig. 9).

4.2. Geomorphological evidence

From the acoustic data, the extent and geomorphology of the presumed lake basin were reconstructed (Fig. 2D). Based on these data, the lake sediments are thought to have occupied an estimated area of ~68.8 km^2 and to have produced a (preserved) volume of ~0.74 km^3 of sediments that accumulated in an isolated bowl-shaped depression. The base of the lake sediments ranges from 41 to 60 m below LAT, indicating a generally low-relief system with only limited deeper depocentres reaching a maximum depth of 19 m below the present-day seafloor towards the NW. In proglacial and ice-dammed lakes, the deepest points often occur near the glacier-lake interface during glacier retreat (Minowa et al., 2023; Wei et al., 2021). In contrast, in fully developed, overdeepened lakes, maximum depth may shift toward the lake centre (Zhang et al., 2023). However, proglacial lake conditions (e.g., water level, temperature, circulation, and glacier contact) shift as the glacier evolves, making these systems highly dynamic and complex (Sutherland et al., 2020), which might cause their preserved morphologies to deviate from the proposed general conceptual models (Zhang et al., 2023). Therefore, the preserved location of maximum depth in this paleolake cannot be confidently linked to the glacier margin position, as it may have been influenced by dynamic glacier-lake processes.

The creation of the lake can be attributed to several ice-marginal mechanisms. Firstly, overdeepened basins become exposed during glacier recession, forming depressions between the retreating ice front and proglacial meltwater systems (Marren, 2002). These basins may expand as retreat accelerates through enhanced calving (Carrivick and Tweed, 2013; Schomacker and Kjær, 2008) and, once exposed, can be rapidly infilled with meltwater and fine sediment (Cook et al., 2011; Zhang et al., 2023), potentially promoting episodic retreat of grounded ice streams (Kelly and Passchier, 2019). Secondly, subglacial erosion may form enclosed basins through localised overdeepening, a process well documented beneath former ice sheets (Cook and Swift, 2012). Thirdly, ice-marginal lakes may occupy pre-existing topographic lows or isostatic depressions that enlarge during glacier recession (Ashley, 1995; Austermann et al., 2022). Fourthly, buried dead-ice bodies, associated with kettle-hole formation, create small, enclosed depressions that evolve into lakes, often characterised by rapid sedimentation and meltout (Benn and Evans, 2010; Knight, 2009; Reitner, 2007). The limited size of classic kettle basins, typically a few meters to several hundred meters (Eilertsen et al., 2016; Knight, 2009), suggests that larger depressions probably result from processes beyond simple dead-ice meltout. In the absence of diagnostic indicators, all proposed formation mechanisms remain plausible.

4.3. Implications for ice-sheet margins and glaciated landscape evolution

Our mapping and sedimentological analyses reveal the presence of an ice-marginal lake, formed during MIS 3, in the southern North Sea. The timing and sedimentary characteristics of this feature are consistent with regional interpretations of the Dogger Bank Formation (DBF), a deposit historically described as proglacial water-lain sediments of Weichselian age (Cameron et al., 1992; Gatliff et al., 1994; Stoker et al., 2011). Subsequent high-resolution studies have demonstrated the internal complexity of the DBF and proposed its subdivision into Basal, Older and Younger subunits that record a range of glacial and periglacial deposits spanning the Weichselian, generally characterised by stiff clays and silts with an increased sand content in the upper parts (Cotterill et al., 2017a, 2017b; Phillips et al., 2018). Thus, Unit C is correlated with the Older DBF based on similarities in lithological composition, stratigraphic position, and architecture, as discussed below.

Early-Middle Weichselian ice advance and retreat (MIS 4/3)

Multiple ice-lobe oscillations have been proposed for the North Sea Basin during the Weichselian, including during the Ferder Episode (ca. 70 ka BP), the Cape Shore Episode (ca. 29-20 ka BP) and the Bolders Bank Episode (ca. 18-16 ka BP), reflecting a complex pattern and sequence of ice advances and retreats (Carr et al., 2006). Although the precise limits of earlier Weichselian ice in the southern North Sea (MIS 4) are not fully constrained (Carr et al., 2006 and references therein), recent reconstructions for the Late Weichselian (late MIS 3-MIS 2) indicate a more extensive and dynamic ice-sheet footprint than

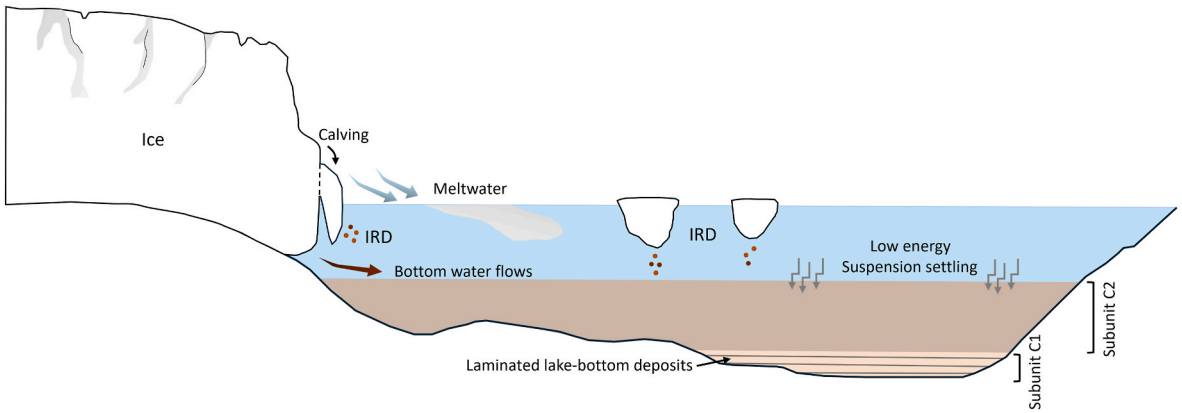


Fig. 9. Schematic representation of ice-proximal sedimentation processes in the MIS 3 lake, showing laminated bottom deposits (subunit C1) overlain by homogeneous mud containing IRD (subunit C2). Sedimentation mechanisms are influenced by meltwater input and bottom-water underflow circulation, adapted from Ashley (1995), Carrivick and Tweed (2013) and Smith and Ashley (1985).

previously recognised (Clark et al., 2012, 2022; Sejrup et al., 2016). Cotterill et al. (2017a,b) attributed deposition of the Basal and Older DBF to an early (pre-LGM) phase of ice expansion, during which ice masses advanced across the area now occupied by the Dogger Bank from the north, east and west and meltwater deposited glacifluvial and glaciolacustrine sediments across a laterally extensive outwash plain (Fig. 10A). Meltwater from retreating ice incised braided outwash channels and likely promoted the deposition of fine-grained glaciolacustrine sediments within small, isolated proglacial lakes and ponds on the exposed surface of the Older DBF (Cotterill et al., 2017a,b). The lake documented in this study (Unit C) is consistent with this model and represents a locally (non-deformed) preserved example of such a ponded meltwater environment (Fig. 10B). In the Dogger region, Roberts et al. (2018) interpreted the Older DBF as a predominantly glaciolacustrine unit associated with the development of a large lake, the so-called Dogger Lake, predating 29.5-26.2 ka (JC123-150VC, 151VC; Roberts et al., 2018). Sediments from this unit show lithological similarities to the lake sediments identified in this study (Unit C; facies *Fm*),

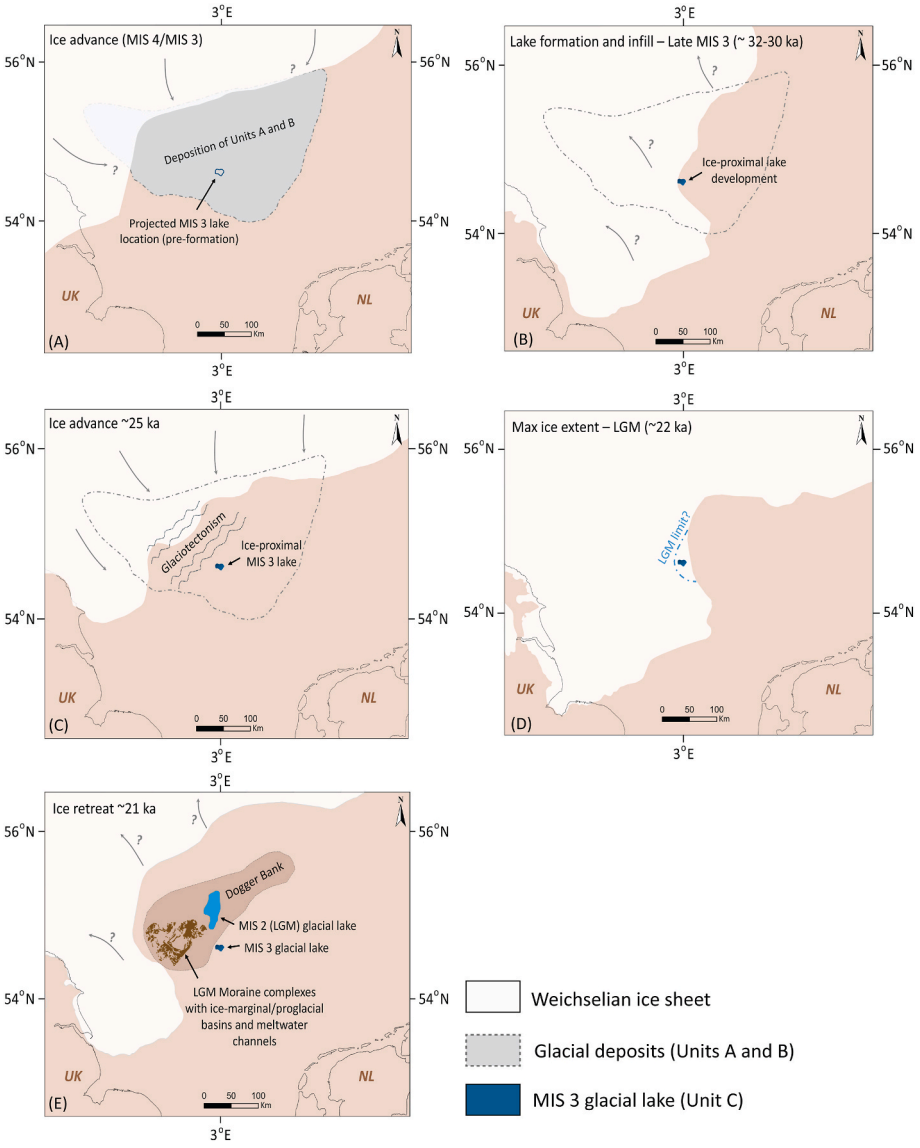


Fig. 10. Proposed landscape reconstruction of Weichselian ice-sheet evolution and associated depositional environments in the southern North Sea. (A) Early-Middle Weichselian (pre-LGM) ice advance from the north, west and east (ice extent by Carr et al., 2006, since MIS 4) established widespread proglacial to glaciolacustrine conditions and deposition of the Basal and Older Dogger Bank formation (Units A and B) (Cotterill et al., 2017a,b; Cameron et al., 1992). The spatial distribution of Units A and B is shown by a grey polygon, combining mapping results from this study with published distributions of the Dogger Bank Formation (British Geological Survey, 1986-1991; TNO-GDN, 2019). (B) Formation and infilling of Lake Waldo identified in this study (Unit C, dark blue polygon) during late MIS 3 over the glaciolacustrine sediments of the Older DBF (grey dashed line). Ice-sheet reconstructions by Clark et al. (2022) indicate BIIS advance into the southern North Sea at ca. 31–32 ka, under which proglacial, ice-marginal lake formation is inferred. Arrows with question marks denote the uncertain direction of subsequent ice retreat, following the lake formation. (C) Later Weichselian ice advance caused glaciotectonic thrusting and folding of the Basal and Older Dogger Bank Formation (grey dashed line), with ice flow from the N–NW (Cotterill et al., 2017a,b; Phillips et al., 2018), although deformation did not reach the study area (ice extent after Clark et al., 2022, ca. 25 ka). (D) During the LGM maximum ice extent, regional reconstructions place the ice margin across the study area (Clark et al., 2022, ca. 22 ka). However, the absence of deformation suggests that the ice margin approached but did not overrun the lake; therefore, a revised local maximum limit is proposed (dashed blue line). (E) Ice retreat (Clark et al., 2022, ca. 21 ka) exposed the glaciated Dogger Bank landscape with thrust-moraine complexes, ice-marginal basins and meltwater systems. Within this landscape, the ice-marginal MIS 3 Lake Waldo identified here (dark blue polygon), together with the LGM proglacial lake described by Emery et al. (2019) and Cotterill et al. (2017a,b) (light blue polygon) formed part of a wider network of ice-proximal and proglacial infill basins. Arrows with question marks indicate inferred directions of post-LGM ice retreat.

comprising stiff, massive, fine-grained sediments (JC123-171VC; Roberts et al., 2018). Based on these similarities, the glaciolacustrine sediments described by Roberts et al. (2018), attributed to the older DBF, are considered to originate from units equivalent to either Unit B or Unit C (as defined in this study) on Dogger Bank, but a definitive correlation cannot be established. Even though no ground-truth data were acquired from Unit B in this study, no stratigraphic or morphological evidence for a large lake is observed in the investigated area, except for the confined lacustrine deposits associated with Unit C. Overall, OSL ages obtained in this study likewise indicate lake deposition begun prior to 32-30 ka, providing chronological support for correlation with this phase of regional glaciolacustrine sedimentation. Therefore, we interpret the documented MIS 3 Lake Waldo as part of a wider glaciolacustrine system that developed during an earlier Weichselian ice presence in the area, possibly contemporary with the Denekamp interstadial.

In recent Ice-sheet reconstructions (Clark et al., 2022), both optimum and maximum scenarios are presented for the maximum ice extent in the area at ca. 31 ka. In the optimum model, both the BIIS and FIS ice margins remain onshore in Scotland and Norway, respectively (Fig. 1A). The maximum scenario places the BIIS limit offshore, extending southwards across the present Dogger Bank (Fig. 1A and B), whilst the FIS is still located onshore, and both ice sheets remain separate entities. Our findings indicate that only the maximum estimated ice-margin position can account for the identified glaciolacustrine deposits, since an expanded ice sheet capable of generating a ponded meltwater environment is required (Sutherland et al., 2020). This maximum reconstruction is further supported by offshore glacigenic material, consistent with the extent of subglacial tills mapped by Cameron et al. (1992) and inferred to be deposited before 31.6-26.2 ka by Roberts et al. (2018) (JC123-178VC, 179VC). Yet neither reconstruction indicates BIIS-FIS coalescence at this time, given the absence of evidence for ice extending into the Fladen Basin or Norwegian Channel (Sejrup et al., 2016). Although the data presented here do not allow a precise determination of the BIIS-FIS configuration, the dropstones identified in cores DB_VC02 and DB_VC03 are dominated by sandstone, mudstone and limestone (mainly chalk), lithologies widely distributed across the central and southern North Sea basin according to offshore bedrock mapping (British Geological Survey, 2013; EMODnet Geology, 2022). Chalk is well-documented in BGS offshore cores, where chalk-rich pebble assemblages have been interpreted as largely derived from eastern England sedimentary rocks (Cameron et al., 1992), while the Danish sector also contains abundant chalk (Vejbæk et al., 2007), making it a possible source. The assemblage lacks igneous or high-grade metamorphic clasts characteristic of Scandinavian shield sources (Sigmond, 2002), which may indicate limited input from that area, although such a contribution cannot be excluded. Overall, the similarity between the observed clast lithologies and mapped North Sea sedimentary successions supports a plausible regional basin source, with erosion and transport to the study site by glacial processes. Following the deposition of Unit C in late MIS 3 (after ca. 30ka), the ice margin is inferred to have retreated northward across the present-day Dogger Bank, before a final re-advance into the area during the LGM.

Late Weichselian advance and maximum extent (LGM)

The Basal and Older DBF are intensively glaciotectonically deformed units, characterised by ice-marginal folding and thrusting, and together with the large thrust-moraine complex mapped on Dogger Bank, indicate that the area was overridden by a glacial advance from the N/NW during a later stage of the Weichselian glaciation (Cotterill et al., 2017a, b; Phillips et al., 2018) (Fig. 10C). It is this phase of ice advance that created the topographic high that partly underlies the present-day Dogger Bank. South of Dogger Bank, where this study is focused, none of the mapped stratigraphic units show evidence of glacial deformation. In addition, cores DB_VC02 and DB_VC03 from the upper part of the lake display no signs of ice overriding. Glacially advancing ice over proglacial lakes is expected to produce pervasive deformation across sediments (Livingstone et al., 2012), as observed in western Dogger Bank, where subglacial diamictons overlie glaciolacustrine deposits of the Older DBF (Roberts et al., 2018). The undeformed acoustic signatures, the sedimentological evidence and the lack of evidence for subsequent till deposits in our study area suggest that the lake might have been situated very close to the maximum ice margin during the LGM, but was not overridden, contradicting recent LGM reconstructions (Clark et al., 2022) (Fig. 10D). Importantly, the correlation of this lake with the Older DBF, previously recognised as a glaciotectonised glaciolacustrine unit on Dogger Bank (Cotterill et al., 2017a,b; Phillips et al., 2018; Roberts et al., 2018), demonstrates that our site preserves the undeformed equivalent of this formation. This captures MIS 3 proglacial conditions in an area unaffected by glaciotectonic deformation, with evidence limited to small, infilled basins.

Final deglaciation and ice-margin retreat

The Younger DBF forms the stratigraphically highest and least deformed component of the DBF, comprising glacial outwash sediments deposited during the northward retreat of the LGM ice margin (Cotterill et al., 2017a, b; Phillips et al., 2018). Following this framework, glacier retreat and subsequent climatic amelioration produced a glaciated landscape across Dogger Bank, in which low-lying areas between moraine ridges, drainage channels and topographic depressions (e.g., pingos and kettle holes) were progressively infilled by outwash sediments of the Younger DBF. On Dogger Bank, a moraine-dammed proglacial lake (~750 km^2) has been mapped, with multi-staged infills capturing ice-contact and ice-distal depositional phases during the Late Weichselian, mainly infilled by the MIS 2 Botney Cut Formation (Emery et al., 2019). Collectively, these findings suggest that the last Weichselian glacial retreat left behind a landscape characterised by a network of smaller, local proglacial lakes occupying ice-proximal depressions (Fig. 10E). A comparable landscape likely existed during the end of MIS 3 in this sector of the southern North Sea, as evidenced by the preserved infilled basin (Unit C) mapped in this study. The sand- and gravel-dominated basal deposits in core DB_VC01 (Unit D) are interpreted as outwash sediments typical of the Younger DBF and yield an OSL date of ca. 18.5 ka, recording the final phase of ice presence and its subsequent decay south of Dogger Bank. Data from north of Dogger Bank suggest that the Dogger Bank was no longer covered by ice after ca. 23.1 ka (JC123/155VC; Roberts et al., 2018). However, re-advances of the North Sea Lobe occurred west and south of Dogger Bank at ca. 22 ka (Evans et al., 2021), with other reconstructions suggesting that ice remained in this sector until ca. 18-16 ka when the BIIS and FIS decoupled (Carr et al., 2006).

Previous studies hypothesised that an extensive LGM lake developed in the area south of Dogger Bank and the Oyster Ground (Clark et al., 2012; Hjelstuen et al., 2018; Murton and Murton, 2012; Sejrup et al., 2016). The results of this study provide no evidence for a large Late Weichselian lake in the investigated region, and therefore cannot support this interpretation. That said, the existence of such a lake further east or north of Dogger Bank cannot be excluded, as glacial lake outburst floods linked to the drainage of an ice-dammed lake during the Late Weichselian have been hypothesised, with the breaching point located at the northeastern part of Dogger Bank (Hjelstuen et al., 2018). However, the dataset presented in this study does not allow evaluation of this hypothesis.

Postglacial landscape and marine onset

Following deposition of the glaciolacustrine and outwash sediments of Units C and D, the area underwent extensive channel incision, marking a shift to postglacial landscape dynamics. Unit E comprises a series of southward-oriented channels. Detailed mapping of channel morphology, morphometry, and spatial distribution has been carried out in the study area by (Kyriakoudi et al., 2026). Faunal assemblages from Unit E (facies *Fm(s)*, *Fl* and *Smf)* indicate a brackish, mesohaline upper-shoreface setting that gradually transitions upward to polyhaline

conditions (F. Wesselingh, personal communication). This succession reflects the development of low-energy systems, likely deposited in protected lagoonal or tidal environments (De Bruyne et al., 2013) during the early Holocene (mean age ca. 9121 cal a BP). Overlying this, the sandy, shell-rich Unit F (facies *Sm)* records the final transition to fully marine conditions, with fauna characteristic of mid-to inner-shelf euhaline soft-seafloor habitats (Daan and Mulder, 2006) (F. Wesselingh, personal communication) by the Middle to Late Holocene.

5. Conclusion

Detailed integration of high-resolution 2D sub-bottom data with sediment core analyses reveals a previously unrecognised buried glaciolacustrine basin south of Dogger Bank, preserved within the glaciated landscape of the southern North Sea. Based on the combined geomorphological and sedimentological evidence from the dataset presented in this study, the presence of an ice-proximal lake, limited in size, formed through glaciolacustrine ponding associated with an advancing Weichselian ice margin is demonstrated. The massive, fine-grained infill deposits contain randomly oriented outsized clasts of heterogeneous lithologies that can be interpreted as ice-rafted dropstones, indicating sustained ice influence in this sector of the southern North Sea.

Micropaleontological, geochemical, and chronological constraints place deposition of these lake sediments in late MIS 3, most likely during the Denekamp interstadials, predating the LGM. These findings provide evidence of glacial influence in this sector of the southern North Sea, supporting the proposed late MIS 3 maximum model ice reconstruction (ca. 31 ka), which places the ice margin in the study area (Clark et al., 2022). The lack of internal deformation within the glaciolacustrine succession indicates that although LGM ice advanced into the wider region, it did not overrun the infilled basin, consistent with the preservation of Late Weichselian outwash sediments identified in this study. This likely represents the preservation of an undeformed equivalent of the glaciotectonised older Dogger Bank Formation in this sector of the southern North Sea. Combined with previous regional evidence for Weichselian glacial activity from the surrounding area, these observations suggest a landscape dominated by a network of small, ice-marginal basins and ponds during MIS 3 in the wider study area, rather than a single, regionally extensive MIS 2 Weichselian lake as previously proposed south of Dogger Bank.

These results provide direct evidence of buried MIS 3 lake sediments preserved in remarkable detail, demonstrating the value of integrating acoustic and sediment core datasets for resolving and reconstructing palaeolandscapes in the southern North Sea. While the directionality and possible merging of the Weichselian ice margin during MIS 3 cannot be constrained here, dropstone lithologies point to a plausible North Sea basin source, and future provenance analyses could provide more precise insights into sediment sources and ice-margin dynamics.

Declaration of competing interest

The authors declare no competing financial or personal interests. This work was supported by the BELSPO-funded project RV/21/WALDO.

Acknowledgments

This study is part of the BELSPO-funded research project “WALDO” (Where are All the (proglacial) Lake seDiments in the NOrth Sea Basin?) led by the Flanders Marine Institute (VLIZ) and Renard Centre of Marine Geology (RCMG) of Ghent University (project RV/21/WALDO). Ship time on *RV Belgica* was provided by BELSPO and RBINS-OD Nature. We thank the crew and technicians of *RV Belgica* for their support during data acquisition. We are grateful to Dr. Soetkin Vervust (Vrije Universiteit Brussel) for assistance with sampling and OSL profiling, Dr. Aayush Srivastava (University of St Andrews) for OSL dating, Anke Demey for grain-size analyses conducted as part of her Bachelor's thesis (Ghent University), and Kamill Lisson and Prof. Dr. Maarten Van Daele (Ghent University) for advice on CT scanning and visualisation. Dr. Rick Hennekam and Jeroen Kooijman are acknowledged for their support during XRF scanning and processing of raw measurements at theRoyal Netherlands Institute for Sea Research (NIOZ). We also thank Dr. Stijn Dewaele (Ghent University) for lithological investigation of the dropstones and Prof. Dr. Frank Wesselingh (Naturalis) for guidance on the interpretation of malacological observations. This study has been conducted using E.U. Copernicus Marine Service Information - https://doi.org/10.48670/moi-00054. The bathymetric data have been derived from the EMODnet Bathymetry portal - http://www.emodnet-bathymetry.eu.

Appendix A. Supplementary data

Supplementary data to this article can be found online at https://doi.org/10.1016/j.quascirev.2026.110190.

Data availability

All data and/or code is contained within the submission.

References

Adamson, K., Lane, T., Carney, M., Bishop, T., Delaney, C., 2019. High-resolution proglacial lake records of pre-Little Ice Age glacier advance, northeast Greenland. Boreas 48 (3), 535–550. https://doi.org/10.1111/bor.12361.

Alho, P., Baker, V.R., Smith, L.N., 2010. Paleohydraulic reconstruction of the largest Glacial Lake Missoula draining(s). Quat. Sci. Rev. 29 (23–24), 3067–3078. https://doi.org/10.1016/J.QUASCIREV.2010.07.015.

Andresen, K.J., Hepp, D.A., Keil, H., Spiess, V., 2022. Seismic morphologies of submerged late glacial to Early Holocene landscapes at the eastern Dogger Bank, central North Sea Basin - implications for geo-archaeological potential. Geol. Soc. Spec. Publ. 525 (1), 13–42. https://doi.org/10.1144/SP525-2021-155.

Aquino, C.D., Milana, J.P., Faccini, U.F., 2014. New glacial evidences at the Talacasto paleofjord (Paganzo basin, W-Argentina) and its implications for the paleogeography of the Gondwana margin. J. South Am. Earth Sci. 56, 278–300. https://doi.org/10.1016/j.jsames.2014.09.001.

Arnaud, E., Martini, I.P., 2009. Glaciations, pre-Quaternary. In: Gornitz, V. (Ed.), Encyclopedia of Paleoclimatology and Ancient Environments. Springer, Netherlands, pp. 384–389. https://doi.org/10.1007/978-1-4020-4411-3_96.

Ashley, G., 1995. Glaciolacustrine environments. Mod. Past Glacial Environ. 1, 335–359. https://doi.org/10.1016/B978-075064226-2/50014-3.

Ashley, G.M., 1988. Classification of glaciolacustrine sediments. In: Genetic Classification of Glacigenic Deposits. Final Report of the Commision on Genesis and Lithology of Glacial Quaternary Deposits of the International Union for Quaternary Research (INQUA), pp. 243–260.

Austermann, J., Wickert, A.D., Pico, T., Kingslake, J., Callaghan, K.L., Creel, R.C., 2022. Glacial isostatic adjustment shapes proglacial Lakes over glacial cycles. Geophys. Res. Lett. 49 (24). https://doi.org/10.1029/2022GL101191 n/a.

Bakke, J., Lie, Ø., Heegaard, E., Dokken, T., Haug, G.H., Birks, H.H., Dulski, P., Nilsen, T., 2009. Rapid oceanic and atmospheric changes during the Younger Dryas cold period. Nat. Geosci. 2 (3), 202–205. https://doi.org/10.1038/ngeo439.

Balascio, N.L., Zhang, Z., Bradley, R.S., Perren, B., Dahl, S.O., Bakke, J., 2011. A multiproxy approach to assessing isolation basin stratigraphy from the Lofoten Islands, Norway. Quat. Res. 75 (1), 288–300. https://doi.org/10.1016/j.yqres.2010.08.012.

Batchelor, C.L., Margold, M., Krapp, M., Murton, D.K., Dalton, A.S., Gibbard, P.L., Stokes, C.R., Murton, J.B., Manica, A., 2019. The configuration of Northern Hemisphere ice sheets through the Quaternary. Nat. Commun. 10 (1). https://doi.org/10.1038/s41467-019-11601-2, 3713-10.

Benn, D.I., Evans, D., 2010. Glaciers & Glaciation, second ed. Hodder Arnold https://www.taylorfrancis.com/books/9781444128390.

Bennett, M.R., Doyle, P., Mather, A.E., 1996. Dropstones: their origin and significance. Palaeogeogr. Palaeoclimatol. Palaeoecol. 121 (3), 331–339. https://doi.org/10.1016/0031-0182(95)00071-2.

Björck, S., 1995. A review of the history of the Baltic Sea, 13.0-8.0 ka BP. Quat. Int. 27 (C), 19–40. https://doi.org/10.1016/1040-6182(94)00057-C.

Blanchet, C.L., Thouveny, N., Vidal, L., 2009. Formation and preservation of greigite (Fe3S4) in sediments from the Santa Barbara Basin: implications for paleoenvironmental changes during the past 35 ka. Paleoceanography 24 (2), n/a. https://doi.org/10.1029/2008PA001719.

Blott, S.J., Pye, K., 2001. GRADISTAT: a grain size distribution and statistics package for the analysis of unconsolidated sediments. Earth Surf. Process. Landf. 26 (11), 1237–1248. https://doi.org/10.1002/esp.261.

Blott, S.J., Pye, K., 2008. Particle shape: a review and new methods of characterization and classification. Sedimentology 55 (1), 31–63. https://doi.org/10.1111/j.1365-3091.2007.00892.x.

Bozzano, G., Cerredo, M.E., Remesal, M., Steinmann, L., Hanebuth, T.J.J., Schwenk, T., Baqués, M., Hebbeln, D., Spoltore, D., Silvestri, O., Acevedo, R.D., Spiess, V., Violante, R.A., Kasten, S., 2021. Dropstones in the Mar del Plata Canyon Area (SW Atlantic): Evidence for Provenance, Transport, Distribution, and Oceanographic Implications. G-cubed : G3 22 (1), n/a. https://doi.org/10.1029/2020GC009333.

Bradley, S.L., Ely, J.C., Clark, C.D., Edwards, R.J., Shennan, I., 2023. Reconstruction of the palaeo-sea level of Britain and Ireland arising from empirical constraints of ice extent: implications for regional sea level forecasts and North American ice sheet volume. J. Quat. Sci. 38 (6), 791–805. https://doi.org/10.1002/jqs.3523.

Bradley, S.L., Milne, G.A., Shennan, I., Edwards, R., 2011. An improved glacial isostatic adjustment model for the British Isles. J. Quat. Sci. 26 (5), 541–552. https://doi.org/10.1002/jqs.1481.

Bradwell, T., Stoker, M.S., Golledge, N.R., Wilson, C.K., Merritt, J.W., Long, D., Everest, J.D., Hestvik, O.B., Stevenson, A.G., Hubbard, A.L., Finlayson, A.G., Mathers, H.E., 2008. The northern sector of the last British Ice Sheet: maximum extent and demise. Earth Sci. Rev. 88 (3), 207–226. https://doi.org/10.1016/j.earscirev.2008.01.008.

British Geological Survey, 2013. BGS offshore bedrock 250k version 3.0. Br. Geol. Surv. https://doi.org/10.5285/d933077d-d8af-48cd-85ba-8c31ce2a95a6 *(Dataset)*.

British Geological Survey (1986-1991). 1:250 000 Geological maps of the UK and continental shelf areas (map sheets California, Swallow Hole, Silver Well and Dogger). Accessed on 17-September-2022.

Bronk Ramsey, C., 2009. Bayesian analysis of radiocarbon dates. Radiocarbon 51 (1), 337–360. https://doi.org/10.1017/S0033822200033865.

Cameron, T.D.J., Crosby, A., Balson, P.S., Jeffery, D.H., Lott, G.K., Bulat, J., Harrison, D. J., 1992. The Geology of the Southern North Sea. United Kingdom Offshore Regional Report. HMSO for the British Geological Survey. T. D. J. Cameron & British Geological Survey., Eds.) [Book].

Cameron, T.D.J., Stoker, M.S., Long, D., 1987. The history of Quaternary sedimentation in the UK sector of the North Sea basin. J. Geol. Soc. 144 (1), 43–58. https://doi.org/10.1144/gsjgs.144.1.0043.

Carlson, A.E., Stoner, J.S., Donnelly, J.P., Hillaire-Marcel, C., 2008. Response of the Southern Greenland ice sheet during the last two deglaciations. Geology (Boulder) 36 (5), 359–362. https://doi.org/10.1130/G24519A.1.

Carr, S.J., Holmes, R., van der Meer, J.J.M., Rose, J., 2006. The last glacial maximum in the North Sea basin: micromorphological evidence of extensive glaciation. J. Quat. Sci. 21 (2), 131–153. https://doi.org/10.1002/jqs.950.

Carrivick, J.L., Chase, S.E., 2011. Spatial and temporal variability of annual glacier equilibrium line altitudes in the Southern Alps, New Zealand. N. Z. J. Geol. Geophys. 54 (4), 415–429. https://doi.org/10.1080/00288306.2011.607463.

Carrivick, J.L., Tweed, F.S., 2013. Proglacial lakes: character, behaviour and geological importance. Quat. Sci. Rev. 78, 34–52. https://doi.org/10.1016/j.quascirev.2013.07.028.

Clark, C.D., Ely, J.C., Fabel, D., Bradley, S.L., 2022. BRITICE-CHRONO maps and GIS data of the last British-Irish Ice Sheet 31 to 15 ka, including model reconstruction, geochronometric age spreadsheet, palaeotopographies and coastline positions. PANGAEA. https://doi.org/10.1594/PANGAEA.945729.

Clark, C.D., Evans, D.J.A., Khatwa, A., Bradwell, T., Jordan, C.J., Marsh, S.H., Mitchell, W.A., Bateman, M.D., 2004. Map and GIS database of glacial landforms and features related to the last British Ice Sheet. Boreas 33 (4), 359–375. https://doi.org/10.1111/j.1502-3885.2004.tb01246.x.

Clark, C.D., Hughes, A.L.C., Greenwood, S.L., Jordan, C., Sejrup, H.P., 2012. Pattern and timing of retreat of the last British-Irish Ice Sheet. Quat. Sci. Rev. 44, 112–146. https://doi.org/10.1016/J.QUASCIREV.2010.07.019.

Cohen, K.M., Gibbard, P.L., Weerts, H.J.T., 2014. North Sea palaeogeographical reconstructions for the last 1 Ma. Neth. J. Geosci. 93 (1–2), 7–29. https://doi.org/10.1017/njg.2014.12.

Conolly, J.R., Ewing, M., 1965. Ice-rafted detritus as a climatic indicator in Antarctic deep-sea cores. Sci. (Am. Assoc. Adv. Sci.) 150 (3705), 1822–1824. https://doi.org/10.1126/science.150.3705.1822.

Cook, S.J., Graham, D.J., Swift, D.A., Midgley, N.G., Adam, W.G., 2011. Sedimentary signatures of basal ice formation and their preservation in ice-marginal sediments. Geomorphology 125 (1), 122–131. https://doi.org/10.1016/j.geomorph.2010.08.018.

Cook, S.J., Swift, D.A., 2012. Subglacial basins: their origin and importance in glacial systems and landscapes. Earth Sci. Rev. 115 (4), 332–372. https://doi.org/10.1016/J.EARSCIREV.2012.09.009.

Cotterill, C., Phillips, E., James, L., Forsberg, C., Tjelta, T.I., 2017a. How understanding past landscapes might inform present-day site investigations: a case study from Dogger Bank, southern central North Sea. Near Surf. Geophys. 15 (4), 403–414. https://doi.org/10.3997/1873-0604.2017032.

Cotterill, C., Phillips, E., James, L., Forsberg, C.F., Tjelta, T.I., Carter, G., Dove, D., 2017b. The evolution of the Dogger Bank, North Sea: a complex history of terrestrial, glacial and marine environmental change. Quat. Sci. Rev. 171, 136–153. https://doi.org/10.1016/j.quascirev.2017.07.006.

Cresswell, A.J., Carter, J., Sanderson, D.C.W., 2018. Dose rate conversion parameters: Assessment of nuclear data. Radiat. Meas. 120, 195–201. https://doi.org/10.1016/j.radmeas.2018.02.007.

Daan, R., Mulder, M., 2006. The Macrobenthic Fauna in the Dutch Sector of the North Sea in 2005 and a Comparison with Previous Data. Numbers 2006–3).

Davies, S.J., Lamb, H.F., Roberts, S.J., 2015. Micro-XRF core scanning in palaeolimnology: recent developments [bookitem]. In: Croudace, I.W., Rothwell, R. G. (Eds.), Micro-XRF Studies of Sediment Cores. Springer, Netherlands, pp. 189–226. https://doi.org/10.1007/978-94-017-9849-5_7.

De Bruyne, R., Van Leeuwen, S., Gmelig Meyling, A., Daan, R., 2013. Schelpdieren van het Nederlandse Noordzeegebied. Ecologische atlas van de mariene weekdieren (Mollusca). Tirion Natuur, Stichting Anemoon, 414.

De Wet, G.A., Balascio, N.L., D'Andrea, W.J., Bakke, J., Bradley, R.S., Perren, B., 2018. Holocene glacier activity reconstructed from proglacial lake Gjøavatnet on Amsterdamøya, NW Svalbard. Quat. Sci. Rev. 183, 188–203. https://doi.org/10.1016/j.quascirev.2017.03.018.

Ehlers, J., 1990. Reconstructing the dynamics of the North-west European Pleistocene ice sheets. Quat. Sci. Rev. 9 (1), 71–83. https://doi.org/10.1016/0277-3791(90)90005-U.

Ehlers, J., Linke, G., 1989. The origin of deep buried channels of Elsterian age in Northwest Germany. J. Quat. Sci. 4 (3), 255–265. https://doi.org/10.1002/jqs.3390040306.

Eilertsen, R.S., Bøe, R., Hermanns, R., Longva, O., Dahlgren, S., 2016. Kettle holes, "dead-ice" topography and eskers on a lake floor in Telemark, southern Norway. Atlas. Submar. Glacial Landf.: Mod. Quat. Anc. 46 (1), 113–114. https://doi.org/10.1144/M46.44.

Emery, A., Hodgson, D., Barlow, N., Carrivick, J., Cotterill, C., Phillips, E., 2019. Left high and dry: deglaciation of Dogger Bank, North Sea, recorded in proglacial lake evolution. Front. Earth Sci. 7. https://doi.org/10.3389/feart.2019.00234.

EMODnet Geology, 2022. EMODnet seafloor geology - sea-floor pre-Quaternary bedrock geology (dataset). Retrieved 2026, from. https://emodnet.ec.europa.eu/geonetwork/srv/eng/catalog.search#/metadata/67b21be525e699400bb33b7ea1f4e672dbb26a33.

Atlantic - European North West Shelf - Ocean Physics Analysis and Forecast. Marine Data Store (MDS). DOI: E.U. Copernicus Mar. Serv. Inf. (CMEMS). Marine Data Store (MDS). https://doi.org/10.48670/moi-00054. (Accessed on *29-December-2023*).

Evans, D.J.A., Roberts, D.H., Bateman, M.D., Clark, C.D., Medialdea, A., Callard, L., Grimoldi, E., Chiverrell, R.C., Ely, J., Dove, D., Ó Cofaigh, C., Saher, M., Bradwell, T., Moreton, S.G., Fabel, D., Bradley, S.L., 2021. Retreat dynamics of the eastern sector of the British-Irish Ice Sheet during the last glaciation. J. Quat. Sci. 36 (5), 723–751. https://doi.org/10.1002/jqs.3275.

Eyles, N., 1987. Late pleistocene debris-flow deposits in large glacial lakes in British Columbia and Alaska. Sediment. Geol. 53 (1–2), 33–57. https://doi.org/10.1016/0037-0738(87)90056-X.

Fairburn, W.A., Bateman, M.D., 2016. A new multi-stage recession model for Proglacial Lake Humber during the retreat of the last British-Irish Ice Sheet. Boreas 45 (1), 133–151. https://doi.org/10.1111/bor.12140.

Fritz, M., Unkel, I., Lenz, J., Gajewski, K., Frenzel, P., Paquette, N., Lantuit, H., Körte, L., Wetterich, S., 2018. Regional environmental change versus local signal preservation in Holocene thermokarst lake sediments: a case study from Herschel Island, Yukon (Canada). J. Paleolimnol. 60 (1), 77–96. https://doi.org/10.1007/s10933-018-0025-0.

Fulton, R.J., Pullen, M.J.L.T., 1969. Sedimentation in upper arrow lake, British Columbia. Can. J. Earth Sci. 6 (4), 785–791. https://doi.org/10.1139/e69-075.

Gatliff, R.W., Richards, P.C., Smith, K., Graham, C.C., McCormack, M., Smith, N.J.P., Jeffery, D., Long, D., Cameron, T.D.J., Evans, D., Stevenson, A.G., Bulat, J., Ritchie, J.D., 1994. United Kingdom Offshore Regional Report: the Geology of the Central North Sea. HMSO for the British Geological Survey, London.

Gibbard, P., Cohen, K., 2015. Quaternary evolution of the North Sea and the English channel. Proceedings Open Univ. Geol. Soc. 1, 63–74.

Gjerde, M., Bakke, J., D'Andrea, W.J., Balascio, N.L., Bradley, R.S., Vasskog, K., Ólafsdóttir, S., Røthe, T.O., Perren, B.B., Hormes, A., 2018. Holocene multi-proxy environmental reconstruction from lake Hakluytvatnet, Amsterdamøya Island, Svalbard (79.5°N). Quat. Sci. Rev. 183, 164–176. https://doi.org/10.1016/j.quascirev.2017.02.017.

Graham, A.G.C., Stoker, M.S., Lonergan, L., Bradwell, T., Stewart, M.A., 2011. The pleistocene glaciations of the North Sea basin [Bookitem]. In: Ehlers, J., Gibbard, P. L., Hughes, P.D. (Eds.), Developments in Quaternary Science. Elsevier Science & Technology. https://doi.org/10.1016/B978-0-444-53447-7.00021-0, 15, pp. 261–278.

Granoszewski, W., 2003. Late Pleistocene vegetation history and climatic changes at Horoszki Duże, eastern Poland: a palaeobotanical study. Acta Palaeobot. 4, 3–95.

Grimm, E.C., 1991. TILIA and TILIA*GRAPH. Illinois State Museum.

Hambrey, M.J., 1994. Glacial Environments. University of British Columbia Press, Vancouver, p. 296.

Heaton, T.J., Köhler, P., Butzin, M., Bard, E., Reimer, R.W., Austin, W.E.N., Bronk Ramsey, C., Grootes, P.M., Hughen, K.A., Kromer, B., Reimer, P.J., Adkins, J., Burke, A., Cook, M.S., Olsen, J., Skinner, L.C., 2020. Marine20—the marine radiocarbon age calibration curve (0-55,000 cal BP). Radiocarbon 62 (4), 779–820. https://doi.org/10.1017/RDC.2020.68.

Hendy, N.I., 1964. An introductory account of the smaller algae of the British coastal waters. Part V. Bacillariophyceae (Diatoms). Fish. Invest. Series, I,. London.

Hepp, D.A., Warnke, U., Hebbeln, D., Mörz, T., 2017. Tributaries of the Elbe Palaeovalley: features of a hidden palaeolandscape in the German Bight, North Sea. In: Bailey, G.N., Harff, J., Sakellariou, D. (Eds.), Under the Sea: Archaeology and Palaeolandscapes of the Continental Shelf. Springer International Publishing, pp. 211–222. https://doi.org/10.1007/978-3-319-53160-1_14.

Hijma, M.P., Cohen, K.M., Roebroeks, W., Westerhoff, W.E., Busschers, F.S., 2012. Pleistocene Rhine-Thames landscapes: geological background for hominin occupation of the southern North Sea region. J. Quat. Sci. 27 (1), 17–39. https://doi.org/10.1002/jqs.1549.

Hjelstuen, B.O., Sejrup, H.P., Valvik, E., Becker, L.W.M., 2018. Evidence of an ice-dammed lake outburst in the North Sea during the last deglaciation. Mar. Geol. 402, 118–130. https://doi.org/10.1016/j.margeo.2017.11.021.

Hounsfield, G.N., 1973. Computerized transverse axial scanning (tomography): Part 1. Description of system. Br. J. Radiol. 46 (552), 1016–1022.
Hughes, A.L.C., Gyllencreutz, R., Lohne, Ø.S., Mangerud, J., Svendsen, J.I., 2016. The last Eurasian ice sheets - a chronological database and time-slice reconstruction, DATED-1. Boreas 45 (1), 1–45. https://doi.org/10.1111/bor.12142.
Jennings, B.R., Parslow, K., 1988. Particle size measurement: the equivalent spherical diameter. Proc. R. Soc. Lond., Ser. A Math. Phys. Sci. 419 (1856), 137–149. https://doi.org/10.1098/rspa.1988.0100.
Jensen, J.B., Bennike, O., Witkowski, A., Lemke, W., Kuijpers, A., 1997. The Baltic Ice Lake in the southwestern Baltic: sequence-, chrono- and biostratigraphy. Boreas 26 (3), 217–236. https://doi.org/10.1111/j.1502-3885.1997.tb00853.x.
Jin, Z., Wang, S., Shen, J., Zhang, E., Li, F., Ji, J., Lu, X., 2001. Chemical weathering since the Little Ice Age recorded in lake sediments: a high-resolution proxy of past climate. Earth Surf. Process. Landf. 26 (7), 775–782. https://doi.org/10.1002/esp.224.
Kasse, C. (Kees), Bohncke, S.J.P., Vandenberghe, J., 1995. Fluvial periglacial environments, climate and vegetation during the middle Weichselian in the northern Netherlands, with special reference to the Hengelo Interstadial. Meded. Rijks Geol. Dienst 52, 387–413.
Kelly, A.L., Passchier, S., 2019. Corrigendum to "A sub-millennial sediment record of ice-stream retreat and meltwater storage in the Baltic Ice Lake during the Bølling-Allerød interstadial" [Quat. Sci. Rev. 198 (2018) 126-139]. Quat. Sci. Rev. 223, 105940. https://doi.org/10.1016/j.quascirev.2019.105940.
Knight, P.G., 2009. In: Gornitz, V. (Ed.), Encyclopedia of Paleoclimatology and Ancient Environments. Springer, Netherlands, pp. 483–484. https://doi.org/10.1007/978-1-4020-4411-3_119. Kettles.
Krammer, K. & Lange-Bertalot, H. (1986-1991): Bacillariophyceae. Naviculaceae, Vol. 2/1, 876 pp.; *Bacillariaceae, Epithemiaceae, Surirellaceae, Vol. 2/2, 596 pp.; Centrales, Fragilariaceae, Eunotiaceae, Vol. 2/3, 576 pp.; Achnanthaceae, Vol. 2/4*, 437 *pp. - In:* Ettl, H.; Gerloff, J.; Heynig, H. & Mollenhauer, D. (eds): Sűβwasserflora von Mitteleuropa. - G. Fisher, Stuttgart. New York. (n.d.).
Kristensen, T.B., Huuse, M., Piotrowski, J.A., Clausen, O.R., 2007. A morphometric analysis of tunnel valleys in the eastern North Sea based on 3D seismic data. J. Quat. Sci. 22 (8), 801–815. https://doi.org/10.1002/jqs.1123.
Kylander, M.E., Ampel, L., Wohlfarth, B., Veres, D., 2011. High-resolution X-ray fluorescence core scanning analysis of Les Echets (France) sedimentary sequence: new insights from chemical proxies. J. Quat. Sci. 26 (1), 109–117. https://doi.org/10.1002/jqs.1438.
Kyriakoudi, D., De Batist, M., Vervoort, M., Mestdagh, T., Missiaen, T., Plets, R., 2026. Multi-criteria characterisation of buried incised valleys and late Quaternary landscape evolution south of Dogger Bank, southern North Sea. Quat. Sci. Rev. 389. https://doi.org/10.1016/j.quascirev.2026.110119.
Lambeck, K., Rouby, H., Purcell, A., Sun, Y., Sambridge, M., 2014. Sea level and global ice volumes from the last glacial maximum to the Holocene. Proc. Natl. Acad. Sci. - PNAS 111 (43), 15296–15303. https://doi.org/10.1073/pnas.1411762111.
Larsen, D.J., Miller, G.H., Geirsdóttir, Á., Thordarson, T., 2011. A 3000-year varved record of glacier activity and climate change from the proglacial lake Hvítárvatn, Iceland. Quat. Sci. Rev. 30 (19), 2715–2731. https://doi.org/10.1016/j.quascirev.2011.05.026.
Larsen, E., Kjær, K.H., Demidov, I.N., Funder, S., GrØsfjeld, K., Houmark-Nielsen, M., Jensen, M., Linge, H., Lysa, A., 2006. Late Pleistocene glacial and lake history of northwestern Russia. Boreas 35 (3), 394–424. https://doi.org/10.1080/03009480600781958.
Lisiecki, L.E., Raymo, M.E., 2005. A Pliocene-Pleistocene stack of 57 globally distributed benthic δ18O records. Paleoceanography 20 (1). https://doi.org/10.1029/2004PA001071.
Livingstone, S.J., Clark, C.D., Piotrowski, J.A., Tranter, M., Bentley, M.J., Hodson, A., Swift, D.A., Woodward, J., 2012. Theoretical framework and diagnostic criteria for the identification of palaeo-subglacial lakes. Quat. Sci. Rev. 53 (C), 88–110. https://doi.org/10.1016/J.QUASCIREV.2012.08.010.
Livingstone, S.J., Ó'Cofaigh, C., Evans, D.J.A., Palmer, A., 2010. Sedimentary evidence for a major glacial oscillation and proglacial lake formation in the Solway Lowlands (Cumbria, UK) during Late Devensian deglaciation. Boreas 39 (3), 505–527. https://doi.org/10.1111/j.1502-3885.2010.00149.x.
López-Buendía, A.M., Bastida, J., Querol, X., Whateley, M.K.G., 1999. Geochemical data as indicators of palaeosalinity in coastal organic-rich sediments. Chem. Geol. 157 (3), 235–254. https://doi.org/10.1016/S0009-2541(98)00207-1.
Mager, S., Fitzsimons, S., 2007. Formation of glaciolacustrine late pleistocene end moraines in the Tasman valley, New Zealand. Quat. Sci. Rev. 26 (5), 743–758. https://doi.org/10.1016/j.quascirev.2006.11.012.
Mangerud, J., 2004. Ice sheet limits in Norway and on the Norwegian continental shelf. Dev. Quat. Sci. 2 (PART 1), 271–294. https://doi.org/10.1016/S1571-0866(04)80078-2.
Marren, P.M., 2002. Glacier margin fluctuations, Skaftafellsjökull, Iceland: implications for sandur evolution. Boreas 31 (1), 75–81. https://doi.org/10.1111/j.1502-3885.2002.tb01057.x.
Martini, I.P., French, H.M., Pérez Alberti, A., 2011. Ice-marginal and periglacial processes and sediments. Geological Society 354. https://doi.org/10.1144/SP354.0.
Martin-Puertas, C., Tjallingii, R., Bloemsma, M., Brauer, A., 2017. Varved sediment responses to early Holocene climate and environmental changes in Lake Meerfelder Maar (Germany) obtained from multivariate analyses of micro X-ray fluorescence core scanning data. J. Quat. Sci. 32 (3), 427–436. https://doi.org/10.1002/jqs.2935.
McCloskey, T.A., Smith, C.G., Liu, K., Marot, M., Haller, C., 2018. How could a freshwater swamp produce a chemical signature characteristic of a saltmarsh? ACS Earth Space Chem. 2 (1), 9–20. https://doi.org/10.1021/acsearthspacechem.7b00098.
Melles, M., Brigham-Grette, J., Minyuk, P.S., Nowaczyk, N.R., Wennrich, V., DeConto, R. M., Anderson, P.M., Andreev, A.A., Coletti, A., Cook, T.L., Haltia-Hovi, E., Kukkonen, M., Lozhkin, A.V., Rosén, P., Tarasov, P., Vogel, H., Wagner, B., 2012. 2.8 million years of Arctic climate change from Lake El'gygytgyn, NE Russia. Sci. (Am. Assoc. Adv. Sci.) 337 (6092), 315–320. https://doi.org/10.1126/science.1222135.
Minowa, M., Schaefer, M., Skvarca, P., 2023. Effects of topography on dynamics and mass loss of lake-terminating glaciers in southern Patagonia. J. Glaciol. 69 (278), 1580–1597. https://doi.org/10.1017/jog.2023.42.
Mitchum Jr, R.M., Vail, P.R., Sangree, J.B., 1977. Seismic stratigraphy and global changes of sea level, Part 6: stratigraphic interpretation of seismic reflection patterns in depositional sequences. Seism. Stratigr. Appl. Hydrocarb. Explor. 26, 117–133.
Moore, P.D., Webb, J.A., Collinson, M.E., 1991. *Pollen Analysis. 2nd Edition,* Blackwell, Oxford, 1-216.
Munyikwa, K., Kinnaird, T.C., Sanderson, D.C.W., 2021. The potential of portable luminescence readers in geomorphological investigations: a review. Earth Surf. Process. Landf. 46 (1), 131–150. https://doi.org/10.1002/esp.4975.
Murray, A.S., Wintle, A.G., 2000. Luminescence dating of quartz using an improved single-aliquot regenerative-dose protocol. Radiat. Meas. 32 (1), 57–73. https://doi.org/10.1016/S1350-4487(99)00253-X.
Murton, D.K., Pawley, S.M., Murton, J.B., 2009. Sedimentology and luminescence ages of Glacial Lake Humber deposits in the central Vale of York. PGA (Proc. Geol. Assoc.) 120 (4), 209–222. https://doi.org/10.1016/J.PGEOLA.2009.09.001.
Murton, D.K., Murton, J.B., 2012. Middle and late pleistocene glacial lakes of lowland Britain and the southern North Sea basin. Quat. Int. 260, 115–142. https://doi.org/10.1016/j.quaint.2011.07.034.
Nesje, A., Bakke, J., Dahl, S.O., Lie, Ø., Bøe, A.-G., 2007. A continuous, high-resolution 8500-yr snow-avalanche record from western Norway. Holocene 17 (2), 269–277. https://doi.org/10.1177/0959683607075855.
Ottesen, D., Dowdeswell, J.A., Bugge, T., 2014. Morphology, sedimentary infill and depositional environments of the early Quaternary North Sea basin (56°-62°N). Mar. Petrol. Geol. 56, 123–146. https://doi.org/10.1016/J.MARPETGEO.2014.04.007.
Phillips, E., Cotterill, C., Johnson, K., Crombie, K., James, L., Carr, S., Ruiter, A., 2018. Large-scale glacitectonic deformation in response to active ice sheet retreat across Dogger Bank (southern central North Sea) during the Last Glacial Maximum. Quat. Sci. Rev. 179, 24–47. https://doi.org/10.1016/j.quascirev.2017.11.001.
Phillips, E., Johnson, K., Ellen, R., Plenderleith, G., Dove, D., Carter, G., Dakin, N., Cotterill, C., 2022. Glacitectonic evidence of ice sheet interaction and retreat across the western part of Dogger Bank (North Sea) during the Last Glaciation. PGA (Proc. Geol. Assoc.) 133 (1), 87–111. https://doi.org/10.1016/j.pgeola.2021.11.005.
Phillips, F.M., Zreda, M.G., Benson, L.V., Plummer, M.A., Elmore, D., Sharma, P., 1996. Chronology for fluctuations in late pleistocene Sierra Nevada glaciers and lakes. Sci. (Am. Assoc. Adv. Sci.) 274 (5288), 749–751. https://doi.org/10.1126/science.274.5288.749.
Pons, A., Beaulieu, J.-L. de, Guiot, J., Reille, M., 1990. Vingt cinq ans de recherches en analyse pollinique. Ecol. Mediterr. 16 (1), 169–193.
Ramirez-Herrera, M.T., Cundy, A., Kostoglodov, V., Carranza-Edwards, A., Morales, E., Metcalfe, S., 2007. Sedimentary record of late-Holocene relative sea-level change and tectonic deformation from the Guerrero Seismic Gap, Mexican Pacific Coast. Holocene 17 (8), 1211–1220. https://doi.org/10.1177/0959683607085127.
Ramírez-Herrera, M.-T., Lagos, M., Hutchinson, I., Kostoglodov, V., Machain, M.L., Caballero, M., Goguitchaichvili, A., Aguilar, B., Chagué-Goff, C., Goff, J., Ruiz-Fernández, A.-C., Ortiz, M., Nava, H., Bautista, F., Lopez, G.I., Quintana, P., 2012. Extreme wave deposits on the Pacific coast of Mexico: Tsunamis or storms? — a multi-proxy approach. Geomorphology 139, 360–371. https://doi.org/10.1016/j.geomorph.2011.11.002.
Ran, E.T.H., 1990. Dynamics of Vegetation and Environment during the Middle Pleniglacial in the Dinkel Valley. The Netherlands.
Reilly, B.T., Stoner, J.S., Wiest, J., 2017. SedCT: MATLAB^{TM} tools for standardized and quantitative processing of sediment core computed tomography (CT) data collected using a medical CT scanner. G-cubed 18 (8), 3231–3240. https://doi.org/10.1002/2017GC006884.
Reitner, J.M., 2007. Glacial dynamics at the beginning of Termination I in the Eastern Alps and their stratigraphic implications. Quat. Int. 164, 64–84. https://doi.org/10.1016/j.quaint.2006.12.016.
Richter, T.O., van der Gaast, S., Koster, B., Vaars, A., Gieles, R., de Stigter, H.C., De Haas, H., van Weering, T.C.E., 2006. The Avaatech XRF Core Scanner: technical description and applications to NE Atlantic sediments. Geol. Soc. Spec. Publ. 267 (1), 39–50. https://doi.org/10.1144/GSL.SP.2006.267.01.03.
Rijsdijk, K.F., Passchier, S., Weerts, H.J.T., Laban, C., van Leeuwen, R.J.W., Ebbing, J.H. J., 2005. Revised Upper Cenozoic stratigraphy of the Dutch sector of the North Sea Basin: towards an integrated lithostratigraphic, seismostratigraphic and allostratigraphic approach. Neth. J. Geosci. 84 (2), 129–146. https://doi.org/10.1017/S0016774600023015.
Roberts, D.H., Evans, D.J.A., Callard, S.L., Clark, C.D., Bateman, M.D., Medialdea, A., Dove, D., Cotterill, C.J., Saher, M., Cofaigh, C.Ó., Chiverrell, R.C., Moreton, S.G., Fabel, D., Bradwell, T., 2018. Ice marginal dynamics of the last British-Irish ice sheet in the southern North Sea: ice limits, timing and the influence of the Dogger Bank. Quat. Sci. Rev. 198, 181–207. https://doi.org/10.1016/j.quascirev.2018.08.010.
Schomacker, A., Kjær, K.H., 2008. Quantification of dead-ice melting in ice-cored moraines at the high-Arctic glacier Holmströmbreen, Svalbard. Boreas 37 (2), 211–225. https://doi.org/10.1111/j.1502-3885.2007.00014.x.
Scourse, J.D., 2024. The timing and magnitude of the British-Irish Ice Sheet between Marine Isotope Stages 5d and 2: implications for glacio-isostatic adjustment, high relative sea levels and 'giant erratic' emplacement. J. Quat. Sci. 39 (4), 505–514. https://doi.org/10.1002/jqs.3611.

Sejrup, H.P., Clark, C.D., Hjelstuen, B.O., 2016. Rapid ice sheet retreat triggered by ice stream debuttressing; evidence from the North Sea. Geology 44 (5), 355–358. https://doi.org/10.1130/G37652.1.

Sejrup, H.P., Larsen, E., Landvik, J., King, E.L., Haflidason, H., Nesje, A., 2000. Quaternary glaciations in southern Fennoscandia: evidence from southwestern Norway and the northern North Sea region. Quat. Sci. Rev. 19 (7), 667–685. https://doi.org/10.1016/S0277-3791(99)00016-5.

Shipboard Scientific Party, 1995. Site 911. In: Myhre, A.M., Thiede, J., Firth, J.V. (Eds.), Proceedings of the Ocean Drilling Program, Initial Reports, vol. 151. Ocean Drilling Program, pp. 271–318. *et al.*.

Sigmond, E.M.O., 2002. Geological Map, Land and Sea Areas of Northern Europe.

Slemmons, K.E., Medford, A., Hall, B.L., Stone, J.R., McGowan, S., Lowell, T., Kelly, M., Saros, J.E., 2017. Changes in glacial meltwater alter algal communities in lakes of Scoresby Sund, Renland, East Greenland throughout the Holocene: abrupt reorganizations began 1000 years before present. Holocene 27 (7), 929–940. https://doi.org/10.1177/0959683616678468.

Small, D., Berg, S., White, D., 2025. Rapid relative sea-level fall, 8-6 ka, in the Windmill Islands, East Antarctica. Quat. Sci. Rev. 365, 109488. https://doi.org/10.1016/J.QUASCIREV.2025.109488.

Smith, N.D., Ashley, G., 1985. Proglacial lacustrine environment. In: Glacial Sedimentary Environments, vol. 16. SEPM Society for Sedimentary Geology. https://doi.org/10.2110/scn.85.02.0135.

Sneed, E.D., Folk, R.L., 1958. Pebbles in the lower Colorado river, Texas a study in particle morphogenesis. J. Geol. 66 (2), 114–150. https://doi.org/10.1086/626490.

Spratt, R.M., Lisiecki, L.E., 2016. A Late Pleistocene sea level stack. Clim. Past 12 (4), 1079–1092. https://doi.org/10.5194/cp-12-1079-2016.

Stansell, N.D., Abbott, M.B., Rull, V., Rodbell, D.T., Bezada, M., Montoya, E., 2010. Abrupt Younger Dryas cooling in the northern tropics recorded in lake sediments from the Venezuelan Andes. Earth Planet Sci. Lett. 293 (1), 154–163. https://doi.org/10.1016/j.epsl.2010.02.040.

Stansell, N.D., Rodbell, D.T., Abbott, M.B., Mark, B.G., 2013. Proglacial lake sediment records of Holocene climate change in the western Cordillera of Peru. Quat. Sci. Rev. 70, 1–14. https://doi.org/10.1016/j.quascirev.2013.03.003.

Stoker, M.S., Balson, P.S., Long, D., Tappin, D.R., 2011. An Overview of the Lithostratigraphical Framework for the Quaternary Deposits on the United Kingdom Continental Shelf. British Geological Survey. British Geological Survey Research Report, *RR/11/03*.

Sutherland, J.L., Carrivick, J.L., Gandy, N., Shulmeister, J., Quincey, D.J., Cornford, S.L., 2020. Proglacial lakes control glacier geometry and behavior during recession. Geophys. Res. Lett. 47 (19), n/a. https://doi.org/10.1029/2020GL088865.

Sutherland, J.L., Carrivick, J.L., Shulmeister, J., Quincey, D.J., James, W.H.M., 2019. Ice-contact proglacial lakes associated with the last glacial maximum across the southern Alps, New Zealand. Quat. Sci. Rev. 213, 67–92. https://doi.org/10.1016/j.quascirev.2019.03.035.

Sutherland, J.L., Evans, D.J.A., Carrivick, J.L., Shulmeister, J., Rother, H., 2022. A model of ice-marginal sediment-landform development at Lake Tekapo, Southern Alps, New Zealand. Geogr. Ann. Phys. Geogr. 104 (3), 151–182. https://doi.org/10.1080/04353676.2022.2084591.

Teller, J.T., Leverington, D.W., Mann, J.D., 2002. Freshwater outbursts to the oceans from glacial Lake Agassiz and their role in climate change during the last deglaciation. Quat. Sci. Rev. 21 (8–9), 879–887. https://doi.org/10.1016/S0277-3791(01)00145-7.

Thys, S., Van Daele, M., Praet, N., Jensen, B.J.L., Van Dyck, T., Haeussler, P.J., Vandekerkhove, E., Cnudde, V., De Batist, M., 2019. Dropstones in lacustrine sediments as a record of snow avalanches—a validation of the proxy by combining satellite imagery and varve chronology at Kenai Lake (South-Central Alaska). Quaternary 2 (1), 11. https://doi.org/10.3390/quat2010011.

Tjallingii, R., Stattegger, K., Wetzel, A., Van Phach, P., 2010. Infilling and flooding of the Mekong River incised valley during deglacial sea-level rise. Quat. Sci. Rev. 29 (11), 1432–1444. https://doi.org/10.1016/j.quascirev.2010.02.022.

Dogger Bight Formation In: Stratigraphic Nomenclature of the Netherlands, TNO - Geological Survey of the Netherlands. Accessed on 28-09-2022 from http://www.dinoloket.nl/en/stratigraphic-nomenclature/dogger-bight-formation.

Van Daele, M., Bertrand, S., Meyer, I., Moernaut, J., Vandoorne, W., Siani, G., Tanghe, N., Ghazoui, Z., Pino, M., Urrutia, R., & De Batist, M. (2016). Late Quaternary evolution of Lago Castor (Chile, 45.6°S): Timing of the deglaciation in northern Patagonia and evolution of the southern westerlies during the last 17 kyr. Quat. Sci. Rev., 133, 130-146. https://doi.org/10.1016/j.quascirev.2015.12.021.

Hammen, van der, Maarleveld, G.C., Vogel, J.C., Zagwijn, W.H., 1967. Stratigraphy, climatic succession and radiocarbon dating of the Last Glacial in The Netherlands. Geol. Mijnbouw 46 (3), 79–95.

Van der Werff & Huls (1958-1974). Diatomeeënflora van Nederland. Eight parts, published privately by van der Werff, De Hoef (U), The Netherlands.

Vandenberghe, J., van der Plicht, J., 2016. The age of the Hengelo interstadial revisited. Quat. Geochronol. 32, 21–28. https://doi.org/10.1016/J.QUAGEO.2015.12.004.

Vasskog, K., Nesje, A., Støren, E.N., Waldmann, N., Chapron, E., Ariztegui, D., 2011. A Holocene record of snow-avalanche and flood activity reconstructed from a lacustrine sedimentary sequence in Oldevatnet, western Norway. Holocene 21 (4), 597–614. https://doi.org/10.1177/0959683610391316.

Vejbæk, O.V., Bidstrup, T., Britze, P., Erlström, M., Rasmussen, E.S., Sivhed, U., 2007. Chalk depth structure maps, central to eastern North Sea, Denmark. GEUS Bulletin 13, 9–12. https://doi.org/10.34194/geusb.v13.4962.

Vos, P.C., de Wolf, H., 1993. Diatoms as a tool for reconstructing sedimentary environments in coastal wetlands; methodological aspects. Hydrobiologia 269–270 (1), 285–296. https://doi.org/10.1007/BF00028027.

Wei, J., Liu, S., Wang, X., Zhang, Y., Jiang, Z., Wu, K., Zhang, Z., Zhang, T., 2021. Longbasaba Glacier recession and contribution to its proglacial lake volume between 1988 and 2018. J. Glaciol. 67 (263), 473–484. https://doi.org/10.1017/jog.2020.119.

Weltje, G.J., Bloemsma, M.R., Tjallingii, R., Heslop, D., Röhl, U., Croudace, I.W., 2015. Prediction of geochemical composition from XRF core scanner data: a new multivariate approach including automatic selection of calibration samples and quantification of uncertainties. In: Croudace, I.W., Rothwell, R.G. (Eds.), Micro-XRF Studies of Sediment Cores. Springer, Netherlands, pp. 507–534. https://doi.org/10.1007/978-94-017-9849-5_21.

Woillard, G.M., 1978. Grande pile peat bog: a continuous pollen record for the last 140,000 Years. Quat. Res. 9 (1), 1–21. https://doi.org/10.1016/0033-5894(78)90079-0.

Xu, H., Liu, B., Wu, F., 2010. Spatial and temporal variations of Rb/Sr ratios of the bulk surface sediments in Lake Qinghai. Geochem. Trans. GT 11 (1). https://doi.org/10.1186/1467-4866-11-3, 3-3.

Zagwijn, W.H., 1961. Vegetation, climate and radiocarbon datings in the late Pleistocene of The Netherlands- part I: Eemian and the Early Weichselian. Mededelingen Rijks Geologische Dienst Nieuwe serie 14, 15–45.

Zagwijn, W.H., 1974. Vegetation, climate and radiocarbon datings in the late Pleistocene of The Netherlands- part II: Middle Weichselian. Mededelingen Rijks Geologische Dienst, Nieuwe Serie 25 (3), 101–110.

Zhang, T., Wang, W., An, B., 2023. A conceptual model for glacial lake bathymetric distribution. Cryosphere 17 (12), 5137–5154. https://doi.org/10.5194/tc-17-5137-2023.

Zingg, T., 1935. Beitrag zur schotteranalyse *(Doctoral dissertation*. ETH Zurich.